Fault-tolerant quantum architectures based on erasure qubits

Shouzhen Gu [1,2,3] Alex Retzker,[2,4] and Aleksander Kubica [2,1,3,*]
[1]California Institute of Technology, Pasadena, California 91125, USA
[2]AWS Center for Quantum Computing, Pasadena, California 91125, USA
[3]Yale Quantum Institute & Department of Applied Physics, Yale University, New Haven, CT 06520, USA
[4]Racah Institute of Physics, The Hebrew University of Jerusalem, Jerusalem 91904, Givat Ram, Israel

(Received 21 March 2024; accepted 20 December 2024; published 6 March 2025)

The overhead of quantum error correction (QEC) poses a major bottleneck for realizing fault-tolerant computation. To reduce this overhead, we exploit the idea of erasure qubits, relying on an efficient conversion of the dominant noise into erasures at known locations. We start by introducing a formalism for QEC schemes with erasure qubits and express the corresponding decoding problem as a matching problem. Then, we propose and optimize QEC schemes based on erasure qubits and the recently introduced Floquet codes. Our schemes are well suited for superconducting circuits, being compatible with planar layouts. We numerically estimate the memory thresholds for the circuit noise model that includes spreading (via entangling operations) and imperfect detection of erasures. Our results demonstrate that, despite being slightly more complex, QEC schemes based on erasure qubits can significantly outperform standard approaches.

DOI: 10.1103/PhysRevResearch.7.013249

I. INTRODUCTION

Quantum error correction (QEC) and fault-tolerant protocols [1–3] can benefit significantly from an ingenious design of qubits with tailored, often hardware-dependent, noise structure. For instance, a bosonic cat qubit [4–8] exhibits biased Pauli noise. Such noise can be readily exploited, e.g., by an appropriate variant of the surface code [9–15], resulting in greatly increased QEC thresholds and reduced qubit overheads of the associated QEC protocols.

Recently, another type of qubit, often referred to as an *erasure qubit*, has received significant attention. Several theoretical proposals have described how the erasure qubit can be straightforwardly realized with, e.g., neutral atoms [16], trapped ions [17], or superconducting circuits [18–20], as well as several promising proof-of-principle experimental demonstrations [21–25]. The idea behind the erasure qubit is to engineer a qubit in such a way that its dominant noise is detectable erasures [26]. Importantly, the knowledge of locations of erasures can be efficiently leveraged by QEC protocols (that may be based on the surface code) and decoding algorithms, leading to high QEC thresholds and an improved subthreshold scaling of the logical error rate [27–29].

For QEC protocols to benefit from erasure qubits, the following requirements have to be satisfied: (i) a large erasure bias, defined as the ratio of the probability of an erasure to the probability of any other residual error within the computational subspace, (ii) an implementation of standard quantum circuit operations, including state preparation, unitary gates, and readout, in a way that preserves an erasure bias, and (iii) the ability to perform an erasure check capable of reliably detecting erasures without introducing additional errors within the computational subspace. Thus, it appears that approaches based on erasure qubits, compared to the standard ones, are more challenging to implement. However, while there is an additional cost associated with, e.g., a careful design of the erasure check, once these additional building blocks are available, then new possibilities for optimized QEC protocols and fault-tolerant architectures open up.

In this paper, we address the question of designing fault-tolerant architectures that are optimized for and make full use of erasure qubits. We start by introducing a formalism for QEC protocols with erasure qubits and express the corresponding decoding problem as the hypergraph matching problem. This, in turn, allows us to design decoding algorithms, which, in many relevant scenarios, may be based on the matching algorithm [15,30]. We then focus on fault-tolerant architectures and find that erasure qubits are particularly suitable for a recently introduced family of QEC codes, Floquet codes [31,32]. In particular, in one realization of erasure qubits via the dual-rail encoding [33,34], the minimal set of quantum circuit operations necessary to implement Floquet codes consists of state preparation, readout, single-qubit gates, and erasure checks (which also play the role of entangling operations). We discuss possible physical implementations of erasure checks in the context of superconducting circuits. To benchmark our scheme, we numerically estimate the memory thresholds of Floquet codes against circuit noise comprising erasures, Pauli errors, and measurement errors (for readout and erasure checks). Lastly, we analyze

*Contact author: a.kubica@yale.edu

Published by the American Physical Society under the terms of the Creative Commons Attribution 4.0 International license. Further distribution of this work must maintain attribution to the author(s) and the published article's title, journal citation, and DOI.

further optimizations of Floquet codes that lead to the reduced qubit overhead, as well as find the smallest Floquet codes with distance two and four, which require, respectively, 4 and 16 qubits.

II. QEC PROTOCOLS WITH ERASURE QUBITS

Analyzing QEC protocols with erasure qubits poses some challenges. First, modeling each erasure qubit may require at least a three-level system, using two levels to represent the computational subspace and a nontrivial orthogonal space as the erasure subspace. Second, quantum circuit operations might, in principle, introduce correlated coherent errors in the presence of erasures. Consequently, there seems to be little hope for efficient simulation methods akin to the ones used for stabilizer circuits [35,36]. In addition, decoding algorithms do not typically consider erasures and their spread.

In this section, we describe how making certain simplifying assumptions allows us to efficiently decode and simulate QEC protocols with erasure qubits; see Appendix A for a detailed description of our formalism. In particular, we phrase the decoding problem as the hypergraph matching problem.

We emphasize that our formalism and numerical simulations go beyond the paradigm of erasure qubits. Namely, they can be used for QEC schemes with leakage, allowing us to quantify the potential gains from the ability to detect leakage [37–39].

A. Setting the formalism

To describe QEC protocols, we use quantum circuits that consist of the following standard single-qubit (1Q) and two-qubit (2Q) operations: (i) 1Q state preparation (of eigenstates of Pauli operators), (ii) 1Q readout (in any Pauli basis), (iii) 1Q Clifford gates, and (iv) 2Q controlled-Pauli CP gates, where $P \in \{X, Y, Z\}$, as well as the additional operations: (v) 1Q erasure checks, (vi) 1Q erasure reset (or reset, for short), (vii) 2Q projective measurements of Pauli PP operators. We refer to such circuits as *erasure circuits*. In contrast, *stabilizer circuits* consist only of operations (i)–(iv) and (vii). An example of an erasure circuit is presented in Fig. 1.

To simulate QEC protocols, we first need to explicitly include all the erasure locations (where erasures may happen) into erasure circuits and then replace each ideal operation (i)–(vii) by its noisy counterpart. We realize the latter by following a standard procedure of adding appropriate Pauli noise $\mathcal{P}$ after each operation and adding bit-flip noise $\mathcal{N}$ to each outcome (for readout, erasure checks, and projective measurements), as depicted in Table I. To realize the former, we choose to insert one erasure location on each wire between each two consecutive operations (i)–(vii); see Fig. 1(b) for an illustration. The noise strengths could be arbitrary at every location. However, for the purposes of our analysis, we describe the noise by three parameters: e, the erasure rate; p, the Pauli error rate; and q, the classical bit-flip noise rate.

In contrast to standard QEC protocols, with erasure qubits not only do we have Pauli noise that affects quantum circuits but also erasures. Erasures are probabilistic processes happening at erasure locations and taking the state from the computational subspace to some orthogonal subspace, which we refer to as the erasure subspace. Furthermore, erasures can spread (probabilistically) via 2Q operations. We envision the following two scenarios.

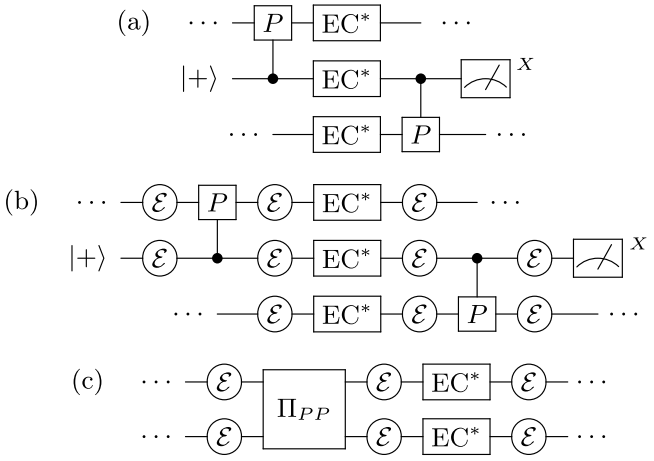


FIG. 1. (a) An erasure circuit consists of standard operations, such as state preparation, readout, and controlled-Pauli gates, as well as erasure checks with reset (denoted by EC*). (b) The same quantum circuit with all possible erasure locations (denoted by $\mathcal{E}$) explicitly inserted. This circuit is used in the ancilla scheme for Floquet codes. (c) The circuit used in the EM scheme for Floquet codes with possible erasure locations inserted.

TABLE I. Mapping of an ideal circuit to a simulated circuit. Note that erasures occur at the locations in-between ideal operations; see Fig. 1(b). For concreteness, we choose $\mathcal{P}(p)$ to be the 1Q or 2Q depolarizing channel (determined by its support) with error rate p, and $\mathcal{N}(q)$ to be the binary symmetric channel (that flips the measurement outcome) with error rate q. In general, $\mathcal{P}$ and $\mathcal{N}$ can represent arbitrary Pauli and binary channels.

operation	ideal	simulated
state preparation	$\|\psi\rangle$ —	$\|\psi\rangle$ — $\mathcal{P}(\frac{3}{2}p)$
readout	P	EC, P, $\mathcal{N}(q)$, $\mathcal{N}(q)$
erasure check with reset	EC*	EC, R, $\mathcal{P}(p)$, $\mathcal{N}(q)$
entangling gate	G	G, $\mathcal{P}(p)$
projective measurement	Π_{PP}	Π_{PP}, $\mathcal{P}(p)$, $\mathcal{N}(q)$

(i) erasure-erasure spread: an erasure spreads to another erasure;

(ii) erasure-Pauli spread: an erasure spreads to a Pauli error.

One concrete realization of the erasure-Pauli spread, which we refer to as the erasure-depolarization spread, is when an erasure spreads to either the identity I, Pauli X, Pauli Y, or Pauli Z, each with probability $\frac{1}{4}$. In other words, any qubit affected by an erasure causes full depolarization of any other qubit that is involved in the same 2Q operation. In the rest of the paper, we focus on the erasure-depolarization spread, as it is the worst-case scenario for erasure-Pauli spread and is a reasonable approximation in certain physical models [40]. The erasure-erasure spread would also be more benign when erasure checks occur after every entangling operation because the erasure information can be obtained from both qubits, effectively decreasing the false-detection rates. For discussion about erasure propagation in the physical model of dual-rail qubits, see Appendix D.

The key part of QEC protocols with erasure qubits is the ability to detect erasures. Erasure detection can be achieved by either readout or erasure checks. Each erasure check performs a nondestructive measurement that distinguishes the states in the computational and erasure subspaces. For simplicity, in our numerical simulations in Secs. IV and V A we assume that each erasure check is immediately followed by reset of the erasure qubit that reinitializes it in the computational subspace (and do not include an erasure location in-between the erasure check and reset). We envision the following two scenarios:

(i) conditional (active) reset that depends on the outcome of the erasure check (and possibly other previous erasure checks);

(ii) unconditional (passive) reset that is independent of any erasure check outcome.

In either case we assume that the erasure qubit is reinitialized in the maximally mixed state in the computational subspace. This is done for concreteness and ease of simulation; reinitializing to a fixed pure state in the computational subspace would give similar results. We further assume that reset acts trivially on the computational subspace. In the rest of the paper we focus on unconditional reset.

We emphasize that in our formalism we assume that the operations (i)–(vii) do not create coherences between the computational and erasure subspaces. This, in turn, allows us to efficiently sample from erasure circuits; see Sec. II C for details. Also, our assumption about the erasure-depolarization spread allows us to push erasures through entangling operations and model entangling operations as always acting on the computational subspace. We leverage this observation to express the decoding problem for erasure circuits as the hypergraph matching problem; see Sec. II B for details.

Our approach generalizes straightforwardly to leakage simulations as long as there are no coherences between the computational and leakage subspaces (regardless of the number of leaked levels), the only difference being the lack of erasure check operations; see Figs. 6(b), 6(e), and 15. When there are coherences, the simulation may become less efficient because we might not be able to use the stabilizer formalism to describe the relevant states.

B. Decoding problem for erasure circuits

Let us first describe the decoding problem for stabilizer circuits. In addition to the stabilizer circuit, we also need to specify a distribution of Pauli errors that are placed at *space-time locations* between operations of the circuit and a set of *detectors* $\{V_i\}$ [41]. By definition, a detector is a product of measurement outcomes in the circuit that is deterministic in the absence of errors and gives information about possible errors when the opposite value is obtained. In this case, we say that the detector is triggered. Detectors may be products of consecutive measurements in the syndrome extraction circuit of a stabilizer code, or they could be more complicated, for example, in a Floquet code. Given detectors which are triggered after running the circuit, the decoding problem is to find a Pauli recovery which undoes the errors that occurred.

The decoding problem for stabilizer circuits can be phrased as a hypergraph matching problem. A hypergraph $H = (V, E)$ is defined by a set of vertices V along with a set of hyperedges E consisting of subsets of vertices (whose sizes can be different than two if H is not a graph). In the hypergraph matching problem of interest, there is a specified set of marked vertices $\nu \subseteq V$ and we wish to find a subset of hyperedges $\tau \subseteq E$ so that its boundary is ν, i.e., $\bigoplus_{\mathcal{T}\in\tau} \mathcal{T} = \nu$, where $\oplus$ denotes the symmetric difference of sets. If the edges are weighted by a function $w : E \to \mathbb{R}$ and multiple solutions are possible, we should find the one with the lowest possible sum of edge weights $\sum_{\mathcal{T}\in\tau} w(\mathcal{T})$.

This formulation is particularly useful in the context of decoding when the distribution of Pauli errors is either equal to or approximated by a product distribution of binary random variables, often referred to as *error mechanisms*. By definition, an error mechanism is a pair (P_i, p_i) such that the Pauli error P_i is inserted at specified space-time locations in the circuit with probability p_i. When P_i occurs, it causes a subset of detectors $\mathcal{T}_i \subseteq \{V_i\}$ to be triggered. If we then define a weighted hypergraph $H = (\{V_i\}, \{\mathcal{T}_i\})$, where each hyperedge $\mathcal{T}_i$ has weight $w(\mathcal{T}_i) = \log[(1 - p_i)/p_i]$, then the problem of finding the most likely error triggering a subset of detectors is exactly the minimum-weight hypergraph matching problem on H described above, for the marked set of vertices $\nu \subseteq \{\mathcal{T}_i\}$ corresponding to the triggered detectors. The recovery operator is the product of all Pauli errors (propagated to the end of the circuit) that correspond to the hyperedges in τ. Even though finding an exact solution to the hypergraph matching problem is in general an NP-hard [42], approximations for decoding certain topological and low-density parity-check codes have been considered [43,44].

The decoding problem for *erasure circuits* is still to find a Pauli recovery. This time, in addition to the triggered detectors, we also have erasure check outcomes. In what follows, we describe a mapping of erasure circuits to stabilizer circuits, where erasures are converted into independent Pauli error mechanisms. This mapping, in turn, allows us to phrase the decoding problem for erasure circuits as a hypergraph matching problem.

We decompose the erasure circuit C_E into *segments*. By definition, a segment s is the world line of a single qubit q

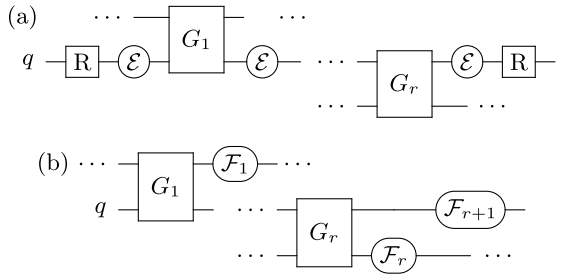


FIG. 2. (a) A segment s of the qubit q in the erasure circuit C_E with entangling operations G_i and erasure locations $\mathcal{E}$. (b) A stabilizer circuit C with space-time locations $\mathcal{F}_i$. By placing space-time correlated Pauli errors at $\overline{\mathcal{F}_i}$ with appropriate probabilities, C becomes equivalent to C_E; see Algorithm 1 for details.

between two consecutive reset operations[1] [see Fig. 2(a) for an illustration]. We also define the entangling operations of s as those with nontrivial support on s and the space-time locations associated with s as those immediately following the entangling operations of s. To map C_E to a stabilizer circuit with independent Pauli error mechanisms, we modify each segment s of C_E by removing the erasure checks and reset operations in s and add appropriate error mechanisms at the locations associated with s. This mapping is guaranteed by Lemma 1.

Lemma 1. Let s be a segment of an erasure circuit C_E. Given the outcomes $\vec{d}$ of erasure checks in s, the distribution of errors introduced by erasures in s is equivalent to a distribution of space-time correlated Pauli errors $\mathcal{P}$ that can be described by independent error mechanisms $\{(P_{i,j}, p_i)\}_{i,j}$. Here, i indexes locations of possible erasures and j indexes the different Pauli strings associated with that erasure.

Proof. The proof proceeds in three steps. First, we find the distribution of Pauli errors caused by erasures in the segment. This distribution can be described by disjoint events which are correlated depolarizing channels applied at different space-time locations in C_E, caused by the erasure-depolarization spread. Second, we show that this distribution can also be described by a product of *independent* events which are space-time correlated depolarizing channels. Third, we decompose each of these space-time correlated depolarizing channels into independent error mechanisms.

We start by introducing some notation. Let G_i be the ith entangling operation in s and $\mathcal{F}_i$ be the space-time location associated with s placed after G_i defined via $\mathrm{supp}\mathcal{F}_i = \mathrm{supp}G_i \setminus \{q\}$, where $i \in \{1, \ldots, r\}$ and q labels the qubit identified with s; see Fig. 2. For convenience, we use G_0 and G_{r+1} to denote the first and second reset operations in s, and define $\mathcal{F}_{r+1}$ to be the location at q after the second reset. In the case when G_i is a 2Q projective measurement, we imagine the classical bit containing the outcome to be a qubit and $\mathcal{F}_i$ to include that qubit. We also define

$$\overline{\mathcal{F}_i} = \bigcup_{j=i}^{r+1} \mathcal{F}_j \,. \tag{1}$$

[1]For brevity, we also refer to state preparation and readout as reset operations.

We want to find the distribution of Pauli errors $\mathcal{P}$ caused by erasures in s. Let A_i be the event that it was first erased at any location in-between G_{i-1} and G_i, where $i \in \{1, \ldots, r+1\}$. When A_i occurs, it causes all qubits connected to q through subsequent entangling operations to be fully depolarized, i.e., fully depolarizing channels are added at space-time locations $\overline{\mathcal{F}_i}$. Note that $\{A_i\}$ are disjoint events. Given the erasure check outcomes $\vec{d}$ (whose probability distribution depends on the erasure probabilities and the false positive and negative detection rates of the erasure checks in the segment s), we can calculate the posterior probabilities

$$a_i = \Pr(A_i|\vec{d}) \,. \tag{2}$$

We then obtain the distribution of Pauli errors $\mathcal{P}$ by sampling disjoint events with probability a_i and inserting fully depolarizing channels at $\overline{\mathcal{F}_i}$ whenever the corresponding event is sampled.

In the description of $\mathcal{P}$, we have disjoint events rather than independent ones. To obtain the desired description, we show that $\mathcal{P}$ can also be obtained by sampling $r+1$ independent events $\{B_i\}$, where B_i is defined as a binary random variable with probability b_i that we soon specify, and placing fully depolarizing channels at space-time locations $\overline{\mathcal{F}_i}$ whenever B_i is sampled. Observe that for $i < j$ a composition of fully depolarizing channels at $\overline{\mathcal{F}_i}$ and $\overline{\mathcal{F}_j}$ is equivalent to the fully depolarizing channels at $\overline{\mathcal{F}_i}$ since $\overline{\mathcal{F}_i} \supseteq \overline{\mathcal{F}_j}$. Therefore, fully depolarizing channels are placed exclusively at $\overline{\mathcal{F}_i}$ iff we sample B_i but no other B_j for $j < i$, which happens with probability

$$b_i \prod_{j=1}^{i-1} (1 - b_j) \,. \tag{3}$$

Equating this with $a_i = \Pr(A_i|\vec{d})$, we see that it suffices to recursively define

$$b_i = a_i \prod_{j=1}^{i-1} (1 - b_j)^{-1} \tag{4}$$

for $1 \leqslant i \leqslant r+1$. Note that $b_i \leqslant 1$ in this definition follows from using induction to show

$$\prod_{j=1}^{i-1} (1 - b_j) = 1 - \sum_{j=1}^{i-1} a_j \tag{5}$$

along with the fact that

$$\sum_{j=1}^{i} a_i = \Pr\left(\bigsqcup_{j=1}^{i} A_i \middle| \vec{d} \right) \leqslant 1 \,. \tag{6}$$

Finally, we further decompose the depolarizing channels resulting from the events $\{B_i\}$ into independent error mechanisms. Namely, for each B_i we introduce $4^{|\overline{\mathcal{F}_i}|} - 1$ error mechanisms, each corresponding to a different nontrivial Pauli error $P_{i,j}$ that can be placed at space-time locations $\overline{\mathcal{F}_i}$ with probability

$$p_i = \tfrac{1}{2} - \tfrac{1}{2}(1 - b_i)^{2^{1-2|\overline{\mathcal{F}_i}|}} \,. \tag{7}$$

ALGORITHM 1. Conversion of an erasure circuit to a stabilizer circuit with independent error mechanisms.

Input:
erasure circuit C_E, erasure check outcomes $\vec{d}$
Output:
stabilizer circuit C, error mechanisms $\{(P_{i,j}, p_i)\}$
$S \leftarrow$ {segments in C_E}
for each $s \in S$ **do**
  $\{\mathcal{F}_i\} \leftarrow$ space-time locations associated with s
  for each i **do**
    $a_i \leftarrow \Pr(A_i|\vec{d})$
    $b_i \leftarrow a_i \prod_{j=1}^{i-1}(1-b_j)^{-1}$
    $p_i \leftarrow \frac{1}{2} - \frac{1}{2}(1-b_i)^{2^{1-2|\overline{\mathcal{F}_i}|}}$
    for each nontrivial Pauli error $P_{i,j}$ at $\overline{\mathcal{F}_i}$ **do**
      include error mechanism $(P_{i,j}, p_i)$
    end for each
  end for each
end for each
$C \leftarrow C_E$ with deleted erasure checks and reset
return C, $\{(P_{i,j}, p_i)\}$

The resulting product distribution of independent error mechanisms $\{(P_{i,j}, p_i)\}$ is equivalent to $\mathcal{P}$. To show that, we use the same reasoning as in claim 1 of Ref. [45]. The analysis there considered Pauli errors on m qubits which occur at the same time, but the only necessary ingredient is that the set of possible errors under composition forms a group isomorphic to $\mathbb{Z}_2^{2m}$ which is true in our case with $m = |\overline{\mathcal{F}_i}|$. This concludes the proof. ■

For the reader's convenience, we recap the conversion of an erasure circuit into a stabilizer circuit with independent error mechanisms in Algorithm 1.

We finish this section with a few remarks.

(i) Depolarizing noise can be decomposed into independent error mechanisms [45]. For arbitrary Pauli channels an exact decomposition may not exist, but one may use an approximate one [44].

(ii) In many scenarios, e.g., the surface code or Floquet codes, the distribution of Pauli errors can be further approximated by a product of independent error mechanisms that trigger at most two detectors. Consequently, the decoding problem reduces to the graph matching problem, which is efficiently solvable [46].

(iii) The number of error mechanisms added for each segment s in Algorithm 1 is exponential in the length of s. If reset operations occur at constant time intervals in the erasure circuit C_E, then the total number of added error mechanisms is proportional to the size of C_E.

(iv) If reset operations occur between every entangling operation in the erasure circuit (as is the case in our numerical simulations), then the resulting error mechanisms are not time correlated and can simply be described by depolarizing channels; see Appendix B.

(v) For simplicity, we focused on the scenario of the erasure-depolarization spread. The analysis for the deterministic erasure-erasure spread is similar. However, the probability of erasure between entangling operations may need to be conditioned on many erasure check outcomes, not just within one segment.

C. Sampling erasure circuits

We envision two ways of sampling from an erasure circuit for simulation purposes. In the first method, we use one bit of information per qubit to represent its erasure state. This allows us to efficiently simulate erasures, erasure checks, and reset operations by sampling from the correct probabilities and updating these classical data. For the qubits in the computational subspace, we keep track of the stabilizers and update them after standard stabilizer circuit operations using the Gottesman-Knill theorem [35,36]. When a qubit is erased, we randomize measurement outcomes involving it and depolarize qubits that interact with it through entangling operations.

Alternatively, we may simulate the circuit by first sampling all erasure check detection events. Conditioned on the results, we then use the results of Sec. II B to obtain stabilizer circuits that we can sample from. Each independent error mechanism in the resulting circuit can be simulated by adding a classical bit that determines whether or not the corresponding error is applied. However, this is often unnecessary because if the Pauli errors occur at the same time (as is the case for us; see Appendix B), it can be simulated by depolarizing channels. The advantage of this approach is that after obtaining the erasure detection events, the same circuit can be used for sampling and decoding.

III. SCALABLE ARCHITECTURE WITH ERASURE QUBITS

In this section, we describe how a realization of erasure qubits via the dual-rail encoding naturally leads to a fault-tolerant architecture based on Floquet codes (which we briefly overview). Our approach is particularly well suited for superconducting circuits. We also discuss possible hardware implementations of physical operations needed to realize Floquet codes.

A. From erasure qubits to Floquet codes

One of the simplest ways to realize the erasure qubit is via the dual-rail encoding [33,34]

$$|\bar{0}\rangle \mapsto |01\rangle, \quad |\bar{1}\rangle \mapsto |10\rangle, \tag{8}$$

which is particularly well suited for superconducting circuits. Namely, the dominant noise for this quantum computing platform is the amplitude damping noise [47,48] that describes the energy relaxation from the excited state $|1\rangle$ to the ground state $|0\rangle$. A single amplitude damping event can be detected as it maps any state of the erasure qubit to the state $|00\rangle$ which is orthogonal to the computational subspace span$\{|01\rangle, |10\rangle\}$. Consequently, the effective noise afflicting the qubit is dominated by detectable erasures. We remark that a few recent experiments demonstrated the erasure qubit via the dual-rail encoding using either two transmons [24] or two three-dimensional (3D) cavities [23,25].

Observe that a projective measurement of a Pauli $Z_{i1}Z_{i2}$ operator, where $i1$ and $i2$ label two qubits forming the erasure qubit i via the dual-rail encoding, is sufficient to implement

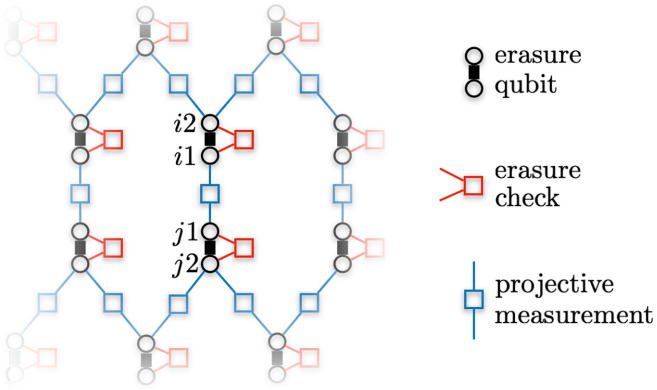


FIG. 3. A planar layout of erasure qubits realized via the dual-rail encoding. Projective measurements of Pauli $Z_{i1}Z_{i2}$ and $Z_{i1}Z_{j1}$ operators implement, respectively, an erasure check for the erasure qubit i and a Pauli $\overline{Z_iZ_j}$ measurement on the computational subspace of two distinct erasure qubits i and j. This layout is well suited for Floquet codes, benefiting from their low-qubit connectivity. The erasure qubit can be realized by two coupled transmons, the erasure check via an LC element [18] and the projective measurement via a single transmon; see Appendix C.

an erasure check; see Fig. 3. Namely, a $+1$ measurement outcome implies that the state is outside the computational subspace span$\{|01\rangle, |10\rangle\}$, and the erasure qubit has suffered from an erasure. However, a projective measurement of a Pauli $Z_{i1}Z_{j1}$ (or $Z_{i2}Z_{j2}$) operator supported on qubits from two different erasure qubits i and j implements a Pauli $\overline{Z_iZ_j}$ measurement on their computational subspace. Therefore, the ability to perform projective measurements of Pauli ZZ operators, together with single-qubit Hadamard $\overline{H}$ and phase $\overline{S}$ gates on the computational subspace, is sufficient to implement erasure checks and Pauli $\overline{XX}$, $\overline{YY}$, $\overline{ZZ}$ measurements on the computational subspace. This, in turn, allows us to implement Floquet codes with erasure qubits (where we implicitly assume the capability of single-qubit state preparation and readout in the computational basis); see Fig. 3 for an illustration.

B. Floquet codes

The foundational idea behind Floquet codes is that encoding information in a dynamically evolving code space may allow for more logical qubits than viewing a set of measurements as defining a static code [31]. Consequently, a Floquet code $\mathcal{C}$ is specified by a sequence of measurements rounds $\mathcal{M}_0, \mathcal{M}_1, \ldots$, where each round $\mathcal{M}_i$ consists of a set of commuting Pauli operators. Note that the operators from $\mathcal{M}_i$ and $\mathcal{M}_j$ may not commute for $i \neq j$. In each round, the code space is a stabilizer code; that is, it is stabilized by an Abelian subgroup of the Pauli group not containing $-I$, which is called the instantaneous stabilizer group (ISG) $\mathcal{S}_i$. Measuring new operators in $\mathcal{M}_i$ takes the previous code space with ISG $\mathcal{S}_{i-1}$ into a new code space stabilized by $\mathcal{S}_i$. The new ISG $\mathcal{S}_i$ is generated by $\mathcal{M}_i$ along with all elements of $\mathcal{S}_{i-1}$ that commute with the new measurements.

The code parameters of a Floquet code $\mathcal{C}$ are as follows. The stabilizer code defined by the ISG $\mathcal{S}_i$ has $k_i \geqslant 0$ logical qubits. The sequence $k_0, k_1, \ldots$ is nonincreasing, and therefore becomes a constant after some number of measurement rounds. We thus define the number of logical qubits of $\mathcal{C}$ to be $k_{\mathcal{C}} = \lim_{i\to\infty} k_i$. The distance of $\mathcal{C}$ should be defined as the circuit distance, i.e., the smallest number of space-time faults that are undetectable yet cause a logical operator to be applied, which depends on the details of the syndrome extraction circuit. For simplicity, we instead consider the distance to be the minimum distance of the stabilizer code from any ISG (which provides an upper bound on the circuit distance).[2]

The first and arguably simplest example of Floquet codes is the honeycomb code [31,32,49], which is defined on a hexagonal lattice with either periodic or open boundary conditions. The honeycomb code is realized by placing qubits on the vertices V and measuring two-qubit Pauli operators associated with the edges E in a specified sequence. Namely, Pauli XX, YY, and ZZ operators are associated with red, blue, and green edges, respectively, and are measured at a round $t \mod 3 = 0, 1, 2$. Since then, many other Floquet codes have been discovered which can realize different topological or fracton phases of matter and have interesting error correction properties [50–57].

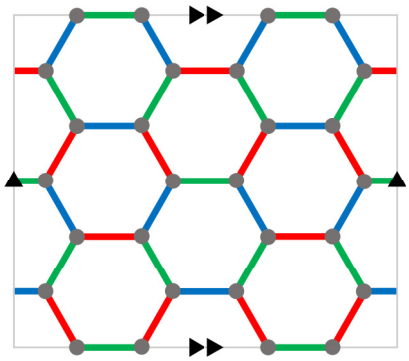
One way to generalize the honeycomb code, which we refer to as a *graph-based* Floquet code, is by defining a QEC code based on a connected graph $G = (V, E)$. We require that the vertices V are 3-regular (i.e., each vertex is incident to three edges) and the edges E are 3-colorable (i.e., the edges split into three sets, $E = E_0 \sqcup E_1 \sqcup E_2$, and no two different edges from E_i are incident). We place qubits on the vertices V and consider a measurement sequence of period three, where at a round $t \mod 3 = 0, 1, 2$ we measure Pauli XX, YY, and ZZ operators associated with edges in E_0, E_1, and E_2, respectively. The definition of graph-based Floquet codes is motivated by the possibility of having a native implementation of two-qubit Pauli measurements with erasure qubits; it also guarantees low-qubit connectivity. We remark that our exhaustive search in Sec. V A finds the smallest graph-based Floquet codes with distance two and four.

We can also consider a Calderbank-Shor-Steane (CSS) version of graph-based Floquet codes, defined using a period-six measurement sequence; see Fig. 4 for an illustration of the CSS honeycomb code [50,52]. In what follows, we mostly focus on CSS Floquet codes, as they outperform the non-CSS counterparts; see Sec. IV.

C. Implementation of erasure checks and Pauli $\overline{ZZ}$ measurements

Floquet codes with erasure qubits crucially rely on three operations: erasure checks, single-qubit gates on the computational subspace, and projective measurements of Pauli $\overline{ZZ}$ operators. Since an erasure check is an extra operation that is not typically considered (on top of state preparation,

[2]Note that the families of Floquet codes considered in Sec. IV have a growing circuit distance which is proportional to the distance. Such scaling of the circuit distance does not hold in general.



round	measure
$t \equiv 0$	X X
$t \equiv 1$	Z Z
$t \equiv 2$	X X
$t \equiv 3$	Z Z
$t \equiv 4$	X X
$t \equiv 5$	Z Z

FIG. 4. A (graph-based) Floquet code can be defined on a hexagonal lattice with periodic boundary conditions. The code is realized via a sequence of measurements of two-qubit Pauli operators (depicted as red, blue, and green edges) on neighboring qubits (gray dots). A sequence of measurements described in the table gives rise to the CSS honeycomb code.

entangling gates, and Pauli measurements), it constitutes an additional hurdle to overcome. We mentioned that for erasure qubits via the dual-rail superconducting encoding erasure checks may, in principle, be realized by a projective measurement of the Pauli operator ZZ, but this is simplistic. Instead, there are efforts to design erasure checks in an optimized way, for instance, by symmetrically coupling a readout resonator to two transmons [18].

Surprisingly, for dual-rail qubits projective measurements of Pauli $\overline{ZZ}$ operators might be efficiently and swiftly realized using a single transmon almost without paying the price for the transmon's low (compared to the dual-rail qubit's) coherence and amplitude damping time T_1. We propose to do so by incorporating the ideas from the cavity dual-rail architecture [19].

Concretely, the parity measurement could be realized by coupling a single transmon (which will be used as an ancilla) to two dual-rail qubits and modulating the flux on the transmon parametrically in resonance with the gaps of the dual-rail qubits; see Fig. 5. Such a modulation realizes the following effective interaction $\frac{g_m}{2} a_5^\dagger a_5 (\overline{Z_1} + \overline{Z_2})$, where g_m is the interaction strength, a_5 is the ladder operator for the ancilla

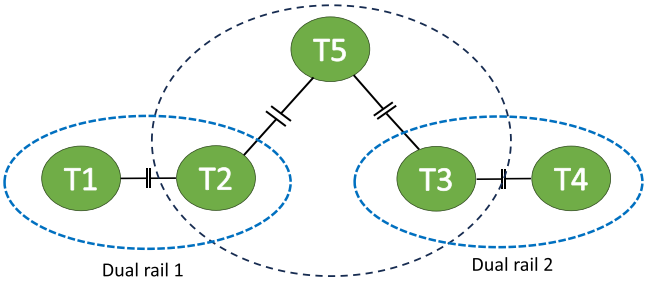


FIG. 5. Scheme for a parity measurement of two dual-rail qubits, which are composed of transmons T1, T2 and T3, T4, respectively. The ancilla transmon T5 is coupled to T2 and T3. In this hardware-efficient construction, the utilization of a coupler is avoided by using T5 for measurement without reducing the efficiency of the procedure. A parity measurement could be realized by modulating the coupler energy gap at the frequency of the dual-rail qubit's gap.

transmon, and $\overline{Z_i}$ denotes Pauli Z operator on the computational subspace of the ith dual-rail qubit. Since the transmon is only coupled to $\overline{Z_1} + \overline{Z_2}$, manipulating the ground and second excited states of the ancilla transmon allows for a robust parity measurement. This method is resilient not only to the phase noise of the ancilla transmon but also to the amplitude damping noise. Assuming that the coherence of the dual rail reaches a few milliseconds [24], the main source of noise in this scheme is expected to be measurement idling dephasing and gate control noise, which both should be less than 10^{-4}; see Appendix C for details. By employing this scheme, we can directly implement the projective measurement of Pauli $\overline{ZZ}$ operators required for Floquet codes.

IV. NUMERICAL SIMULATIONS FOR FLOQUET CODES

We now describe the results of our numerical simulations of Floquet codes with erasure qubits. Our simulations were performed using the second method of sampling described in Sec. II C. After sampling erasure check detection events, we used the Python package STIM [41] to sample from the resulting stabilizer circuits. For each sample, STIM outputs detectors that are violated along with the final value of a given logical operator and decomposes noise into error mechanisms that set off at most two detectors. Thus, we decode using the method outlined in Sec. II B by inputting this decoding graph along with the samples to the minimum-weight perfect matching decoder PYMATCHING [58]. The decoder reports an error if, after decoding, the value of the logical operator is different than when initialized. For a distance d code, we calculate p_L, the logical error rate per $3d$ rounds. For more details of the simulation, see Appendix E.

We simulate two ways of implementing the projective measurements used in Floquet codes: (i) the ancilla scheme using an ancilla qubit and two-qubit entangling gates as depicted in Figs. 1(a) and 1(b) and (ii) the 2Q entangling measurement (EM) scheme as described Sec. III C. In both scenarios we perform either erasure checks with reset or readout after each entangling operation. The circuits simulated for the ancilla and EM schemes are the ones illustrated in Figs. 1(b) and 1(c), respectively, with each ideal operation replaced with its noisy counterpart described in Table I.

Our main numerical results analyzing the CSS honeycomb code are presented in Fig. 6. We probe the (e, p, q) phase space (where e, p, and q are the erasure, Pauli, and measurement error rates, respectively) to determine the threshold surface and find the correctable region where errors can be suppressed arbitrarily by increasing the code distance. We remark that depending on the noise parameters it may be optimal to perform erasure checks less frequently than after every entangling operation. Although we have not simulated all possible erasure check schedules, we find an upper bound for their thresholds by simulating the scheme with ideal erasure checks and reset. In particular, the light blue and orange regions in Figs. 6(b) and 6(e) represent potential gains of the correctable region that may be achieved by optimizing the erasure check schedules. Alternatively, the solid lines could be brought closer to the ideal bound (dashed lines) by simultaneously performing the erasure measurement with the entangling operation and improving the reset procedure.

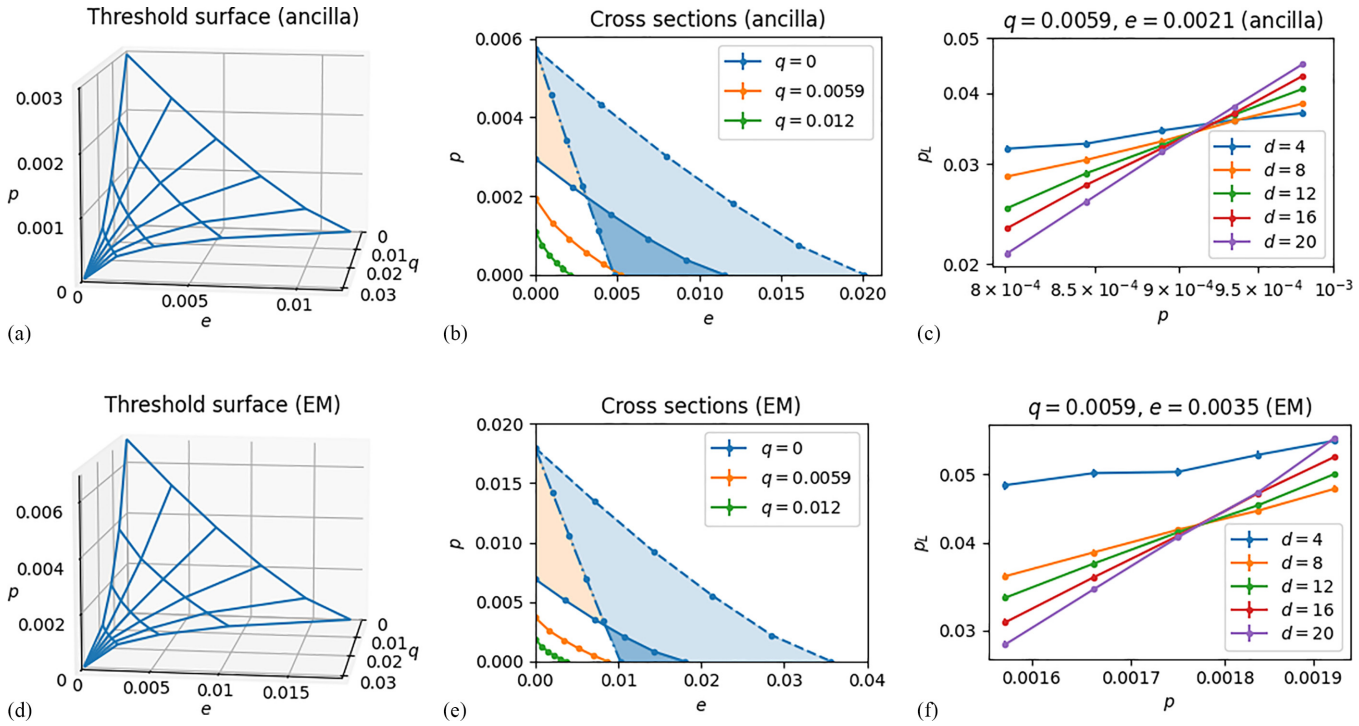


FIG. 6. Simulations of the CSS honeycomb code realized via the (a)–(c) ancilla and (d)–(f) EM schemes. (a), (d) The threshold surface in the (e, p, q) phase space, where e, p, and q are the erasure, Pauli, and measurement error rates, respectively. The threshold values are approximately $e^* = 1.15\%$, $p^* = 0.29\%$, $q^* = 2.97\%$ for the ancilla scheme and $e^* = 1.80\%$, $p^* = 0.69\%$, $q^* = 2.97\%$ for the EM scheme. (b), (e) Cross sections of the threshold surface for different values of q (solid lines). The dashed lines correspond to the scheme with erasure checks and reset that cause no additional errors, bounding the performance of any erasure scheme. The dashed-dotted lines correspond to the standard scheme with no erasure checks and ideal reset (also interpreted as the code's performance under leakage). Erasure schemes can operate in a region (blue) where the standard scheme cannot. Since erasure checks and reset cause additional errors, for a low erasure bias there is a region (orange) where the standard scheme may be better. (c), (f) We find the thresholds by plotting the logical error rate p_L for distance-d codes as a function of p or e, and fitting a finite-size scaling ansatz; see Appendix E.

In Fig. 7, we show how the logical error rate p_L is suppressed by increasing code distance for error rates below threshold in the ancilla and EM schemes. We choose e, p, and q to be in the correctable region for the erasure scheme from Fig. 6. These values are also comparable with the experimentally measured erasure and residual error rates of 0.4% and 0.01% per single-qubit gate, and the false positive and negative erasure detection rates of around 1% [24].

In Fig. 8, we present several optimizations where we find the threshold for the ancilla and EM schemes under erasure-biased noise characterized by a single parameter $x = q = e = 10p$. We consider two layouts: (i) the standard embedding of the hexagonal lattice on a torus as in Fig. 4(a) and (ii) the qubit-efficient layout achieving the same distance by "twisting" the torus as in Fig. 9(f). This qubit-efficient layout, suggested in Refs. [32,59], is the optimal layout on a torus for a given distance and uses 25% fewer qubits than the standard layout [60]. Although the logical error rate p_L at the threshold is lower for the standard layout, at low physical error rates, where the scaling of p_L is determined by the distance, it is preferential to use the compact layout as it achieves a higher distance for a given number of physical qubits. We also simulate the performance of the original honeycomb code with the compact layout and find that its threshold is lower than that of the CSS honeycomb code. This can be explained by the fact that the detectors are products of 6 measurement outcomes in the CSS honeycomb code compared to products of 12 measurement outcomes in the original honeycomb code. Therefore, the CSS version is more robust against measurement errors.

The results of this section can be viewed as an initial step toward realistic simulations of erasure qubits. Although we simulate the honeycomb code on a torus for simplicity, using a planar layout [32,49] more compatible with superconducting hardware should give the same thresholds. The fact that boundary conditions do not affect thresholds is supported by the comparison of the standard and compact layouts in Fig. 8. We also remark that using the three parameters e, p, q is a simplistic way to characterize the noise. In practice, noise from hardware needs to be translated to (possibly varying) erasure, Pauli, and measurement error rates at different locations. Therefore, although e, p, q have the same meaning between the ancilla and EM schemes, the numerical values from the various plots should not be directly compared because implementing the two types of entangling operations requires different hardware setups that would lead to different error rates. Using realistic error parameters would also allow us to calculate the QEC overhead needed to achieve a given logical error rate by extrapolating from a subthreshold scaling plot similar to Fig. 7. (Such an extrapolation should not be done for p_L too small because other effects may dominate.)

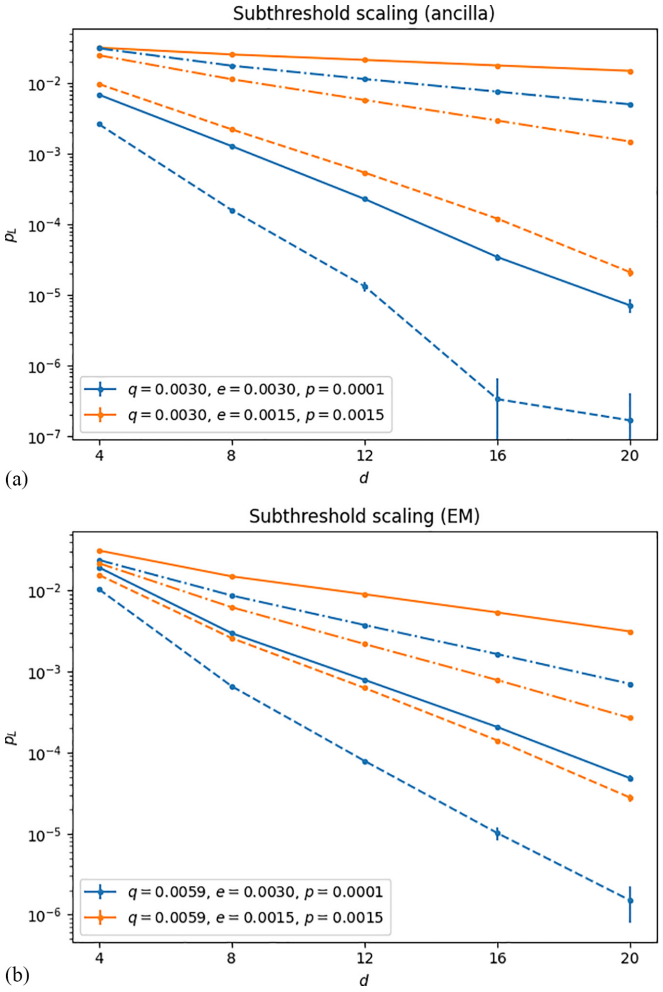


FIG. 7. Subthreshold scaling of the logical error rate p_L with distance d for the (a) ancilla and (b) EM schemes. We compare the results when checking for erasures after every entangling operation (solid), without performing any erasure checks (dashed-dotted), and in an ideal case where erasure checks introduce no errors (dashed), which gives a lower bound on the achievable p_L. For a high erasure bias (blue), we obtain better suppression and scaling of p_L by performing the erasure scheme; for a low erasure bias (orange), the standard scheme is better.

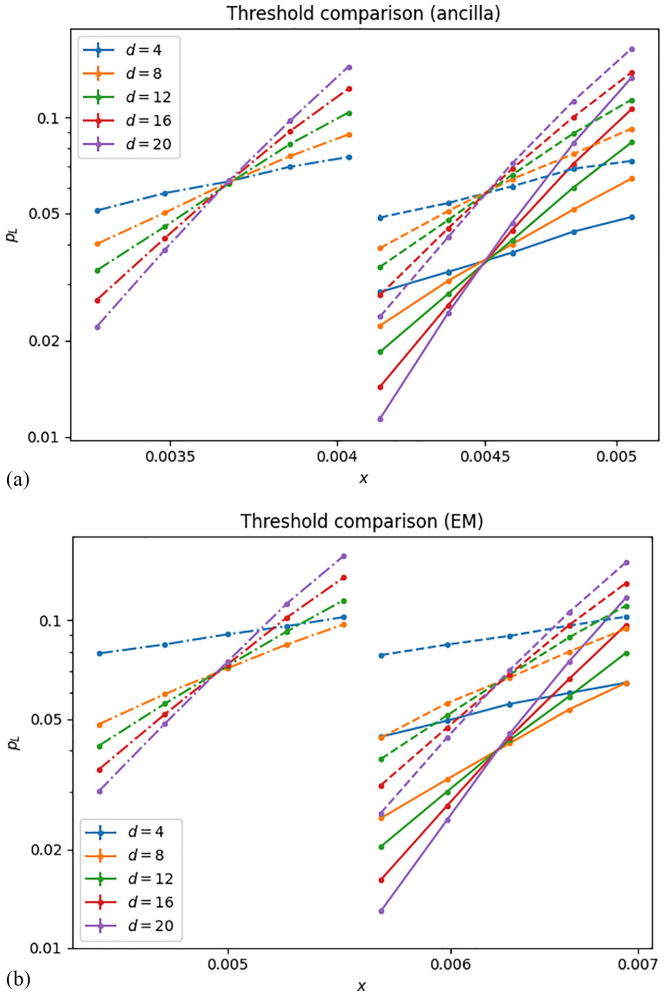


FIG. 8. Comparison of the thresholds for the (a) ancilla and (b) EM schemes. We assume erasure-biased noise with a single parameter $x = q = e = 10p$. For the CSS honeycomb code, the standard (solid) and compact (dashed) layouts give the same threshold, with the latter having higher logical error rate p_L for the same distance d. The original honeycomb code (dashed-dotted) with the compact layout exhibits a lower threshold.

V. SMALLEST FLOQUET CODES

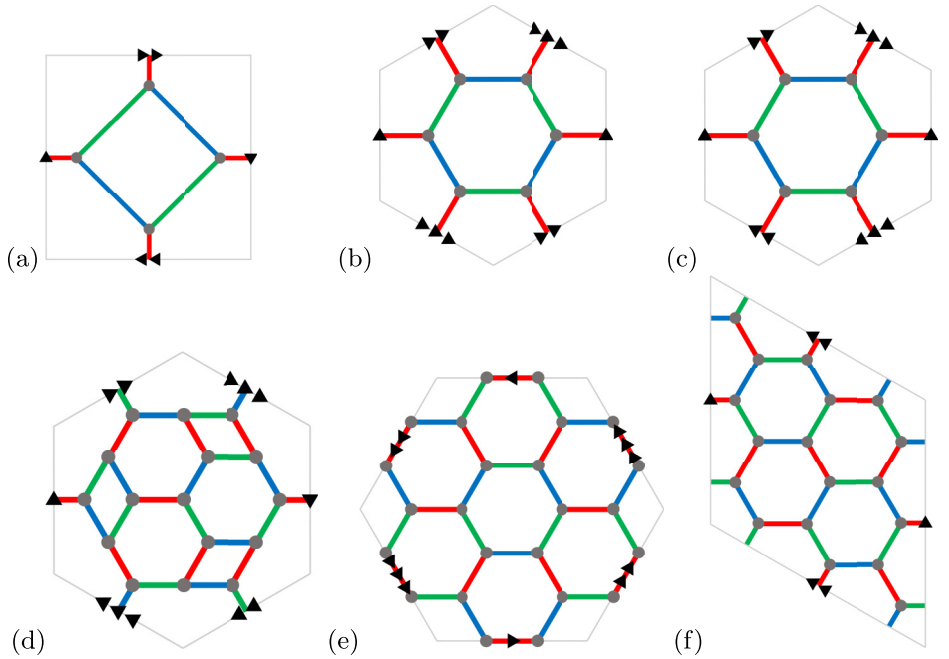
Having analyzed families of Floquet codes on the torus, one may ask what the smallest possible (graph-based) Floquet codes are. In this section, we find the previously unknown codes with distance two and four and analyze their performance in terms of the logical error rate. We also describe a connection between Floquet codes and two-manifolds.

A. Searching for smallest Floquet codes

Because we are considering erasures, distance-two codes may allow us to correct up to one erasure. The smallest 3-regular graphs are the complete graph K_4, the complete bipartite graph $K_{3,3}$, and the prism graph Y_3. Each of these graphs has exactly one 3-edge coloring (up to isomorphism), so they define valid Floquet codes. The codes all have distance two, and they encode either one or two logical qubits. The graphs K_4, $K_{3,3}$, and Y_3 with their edge colorings are depicted in Figs. 9(a)–9(c), respectively. We remark that compared to the $[\![16, 4, 2]\!]$ hyperbolic code defined on the Bolza surface [55], the $[\![6, 2, 2]\!]$ codes defined on $K_{3,3}$ and Y_3 have better encoding rates at the same distance.

For Floquet codes that can correct one unknown error, we consider distance-four codes. Previously, the smallest known Floquet code with distance four was the $[\![18, 2, 4]\!]$ code using the twisted embedding of the hexagonal lattice on a torus [32,59]; see Fig. 9(f). We ran an exhaustive search through all 3-edge colorings of 3-regular graphs up to 18 vertices and found two additional distance-four codes with 16 and 18 qubits. These codes both encode one logical qubit; see Figs. 9(d) and 9(e).

We also simulate the performance of the $[\![16, 1, 4]\!]$ code, presenting the results for the ancilla and EM schemes in Fig. 10. To find the pseudothresholds, we compare the logical error rate p_L of the code against an unprotected qubit that



code	Σ	n	k	d
(a)	$\mathbb{RP}^2$	4	1	2
(b)	$\mathbb{T}^2$	6	2	2
(c)	$\mathbb{K}$	6	2	2
(d)	$\mathbb{RP}^2$	16	1	4
(e)	$\mathbb{RP}^2$	18	1	4
(f)	$\mathbb{T}^2$	18	2	4

FIG. 9. The smallest (graph-based) Floquet codes with distance two and four. Qubits are depicted as gray dots. For each code illustrated in (a)–(f), we specify a manifold Σ used to embed its associated graph, as well as its code parameters n, k, and d. Here, $\mathbb{T}^2$, $\mathbb{RP}^2$, and $\mathbb{K}$ denote a torus, a real projective plane, and a Klein bottle, respectively.

undergoes the same noise and is affected by four depolarizing channels, two with error rate p and two with error rate $3e/4$, at every step. In the EM scheme, there are single error mechanisms that can corrupt two qubits along a logical operator, which halves the circuit distance compared to the distance of the stabilizer code of any ISG. This can be seen from the subthreshold scaling, as the slopes of the solid and dashed lines are the same for low error rates. This phenomenon does not occur for the ancilla scheme.

B. Interpretation through manifolds

It turns out that one can interpret any graph-based Floquet code as arising from a tessellation of some closed two-manifold (with the tessellation forming a two-dimensional color code lattice [61,62]). By definition, a two-dimensional color code lattice is 3-regular and its faces are 3-colorable, i.e., faces are colored with three colors and any two neighboring faces sharing an edge have different colors. The following lemma guarantees the relation between Floquet codes and two-manifolds.

Lemma 2. Any finite connected 3-regular graph $G = (V, E)$ with a 3-edge coloring $E = E_0 \sqcup E_1 \sqcup E_2$ can be embedded in a closed two-manifold Σ with 3-colorable faces, whose coloring is induced by the edge coloring.

Proof. For each i, we may remove all edges in E_i to obtain a disjoint union of cycles. Consider filling in these cycles so that they are homeomorphic to disks, and let F_i denote this collection of disks. The boundaries of the disks are edges of the graph, and each edge in G is part of the boundary of exactly two disks in $F = F_0 \sqcup F_1 \sqcup F_2$. By gluing disks together along an edge when they share the same edge in G, we obtain a closed manifold Σ on which G has a natural embedding. The faces of Σ are F and their coloring is induced by the coloring of the edges of G, i.e., any face in F_i has color i. Note that since each i-colored edge is part of faces colored j and k, with i, j, k all distinct, any two neighboring faces of Σ have different colors (both distinct from i). ■

The parameters of the Floquet code associated with the graph G can be related to the Σ embedding of G. Let us define the shrunk lattice of color i to be the graph $G_i = (F_i, E_i)$, where an edge $e \in E_i$ connecting v to w in the original graph G now connects the two i-colored faces that v and w are on. The graph G_i also has an embedding in Σ, which is obtained from the embedding of G by "shrinking" the i-colored faces to a point and extending the i-colored edges. Similarly to Ref. [31], we find that at every round i of the evolution of the Floquet code, the ISG is equivalent to the toric code on the Σ embedding of G_i. Thus, the number of encoded qubits is

$$k = \dim H_1(\Sigma; \mathbb{Z}_2) = 2 - \chi \tag{9}$$

$$= \begin{cases} 2g, & \text{orientable } \Sigma \text{ of genus } g \\ g, & \text{nonorientable } \Sigma \text{ of demigenus } g \end{cases} \tag{10}$$

where $H_1(\Sigma; \mathbb{Z}_2)$ is the first homology group of the two-manifold Σ with $\mathbb{Z}_2$ coefficients and χ is the Euler characteristic of Σ. Furthermore, the distance of the Floquet code at round i is the smaller of twice the length of the shortest noncontractible cycle of G_i (embedded in Σ) and the length of the shortest noncontractible cycle in the dual graph G_i^*.[3] Since the dual graph G_i^* is bipartite, the distance is even.

[3]The dual graph of an embedded graph has vertices which are faces of the original graph and edges connecting vertices corresponding to adjacent faces.

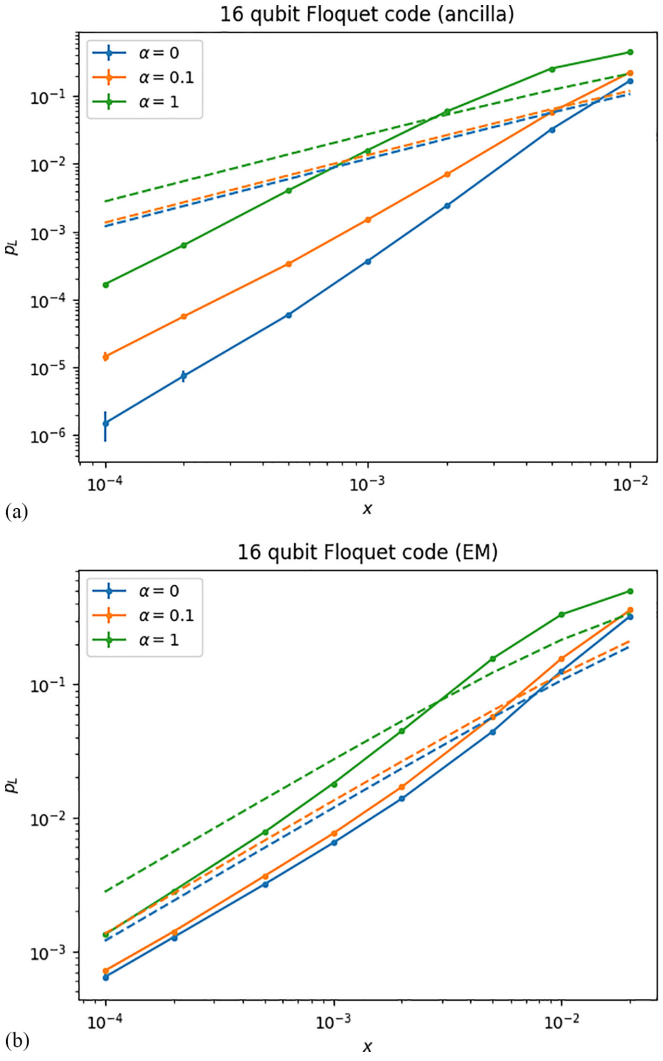


FIG. 10. Finding the pseudothreshold of the $[\![16, 1, 4]\!]$ code in the (a) ancilla and (b) EM schemes. We assume erasure-biased noise with $q = e = x$ and $p = \alpha x$ where x and α are parameters. The dashed lines represent error rates of an unprotected qubit experiencing the same noise while idling for the same amount of time.

VI. DISCUSSION

In our paper, we designed and optimized fault-tolerant quantum architectures based on erasure qubits. While our analysis has focused on Floquet codes, we also envision making use of other QEC codes, such as the surface code and quantum low-density parity-check codes [63]. The surface code, similarly to graph-based Floquet codes, can be realized with planar layouts of qubits and projective measurements of Pauli XX and ZZ operators between neighboring qubits [45,64]; quantum low-density parity-check codes are generally incompatible with planar layouts, but, in principle, can be realized with, e.g., superconducting circuits [65] and neutral atoms [66]. Irrespective of the QEC codes used, we expect the corresponding quantum architectures to benefit from erasure qubits and significantly outperform standard approaches.

A direct comparison of the overhead of using erasure qubits versus standard qubits requires a careful resource count. For example, one should include the number of control lines and the number of resonators needed to implement erasure checks and parity measurements (see Appendix C) on superconducting dual-rail qubits. A subthreshold scaling plot such as Fig. 7 may be used to estimate the resources needed to achieve a desired logical error rate. For example, for $(e, p, q) = (0.003, 0.0001, 0.0059)$ under the EM scheme, $\sim 10^{-3}$ error rate is achieved with distance $d_{\text{eq}} = 12$ using erasure qubits, at least distance $d_{\text{st}} = 20$ using standard qubits, and as small as distance 8 in an ideal scenario with erasure qubits. Therefore, in this crude comparison, where one dual-rail qubit is equivalent to two standard transmon qubits, using erasure qubits requires $2 \times \frac{3}{2} d_{\text{eq}}^2 = 432$ transmons compared to $\frac{3}{2} d_{\text{st}}^2 = 600$ transmons for the standard scheme.

Our analysis and numerical simulations relied on certain simplifying assumptions, including the erasure-depolarization spread, noise rates that are uniform through the circuit, and frequent erasure checks followed by unconditional reset. However, similar analysis can be fine tuned for specific architectures, making it more realistic and potentially further improving the performance of QEC protocols. For instance, if erasures spread to Pauli Z errors, then one may be able to design clever syndrome extraction circuits that suppress the error propagation. One may adjust the noise rate at each space-time location depending on the execution time of quantum circuit operations; see Appendix B for an illustrative example. Also, one may choose to perform less frequent erasure checks (to reduce the time overhead associated with their implementation) and conditional reset operations (to reduce the effect of false negative erasure detections) [40].

Lastly, our formalism for QEC protocols with erasure qubits and phrasing the corresponding decoding problem as the hypergraph matching problem constitute the first step toward systematic development and optimization of decoding algorithms. Such efforts, in turn, will further solidify the claim that erasure qubits are an attractive building block for fault-tolerant quantum architectures.

ACKNOWLEDGMENTS

We thank A. Grimsmo, A. Haim, C. Hann, J. Iverson, and H. Levine for many inspiring discussions. We acknowledge C. Pattison for his help with finding small Floquet codes. S.G. acknowledges funding from the Air Force Office of Scientific Research (Grant No. FA9550-19-1-0360).

APPENDIX A: FORMAL DESCRIPTION OF QEC PROTOCOLS WITH ERASURE QUBITS

We can make the discussion about QEC protocols with erasure qubits more precise. Formally, each wire represents an erasure qubit and it suffices to model it as a three-level system with an orthonormal basis $|0\rangle$, $|1\rangle$, and $|2\rangle$, where the states $|0\rangle$ and $|1\rangle$ span the computational subspace $\mathcal{H}_c \simeq \mathbb{C}^{\otimes 2}$ and the state $|2\rangle$ spans the erasure subspace $\mathcal{H}_e \simeq \mathbb{C}$. Let Π_a and $\Pi_{a,b}$, where $a, b \in \{c, e\}$, denote the projectors onto $\mathcal{H}_a$ and $\mathcal{H}_a \otimes \mathcal{H}_b$, respectively. Similarly, we define $\Pi_P^{\pm}$ and $\Pi_{PP}^{\pm}$, where $P \in \{X, Y, Z\}$, to be the projectors onto the (± 1) eigenspaces of the Pauli P and PP operators, respectively. We write $G_{a,b}$ to capture that the operator G acts on $\mathcal{H}_a \otimes \mathcal{H}_b$.

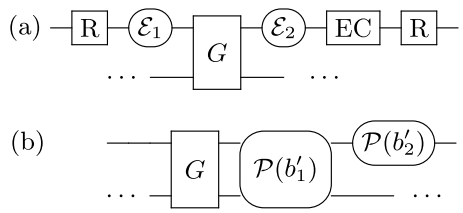


FIG. 11. (a) An example of a segment of an erasure circuit. (b) An equivalent stabilizer circuit.

In Sec. II A we assumed that none of the operations (i)–(vii) can create a superposition of states in the computational and erasure subspaces of erasure qubits. Given our assumption of the erasure-depolarization spread, i.e., an erasure causes full depolarization of another qubit that is involved in the same 2Q operation, we obtain that the operations (i)–(vii) have a block-diagonal structure and act on the Hilbert spaces associated with erasure qubits as follows.

(i) 1Q state preparation of a state $|\psi\rangle \in \mathcal{H}_c$ in the computational subspace of the erasure qubit.

(ii) 1Q readout measures a Pauli P operator, but if the state is erased, then it gives a random outcome, i.e., it performs the two-outcome positive operator-valued measure (POVM) with $\Pi_P^+ + \frac{1}{2}\Pi_e$ and $\Pi_P^- + \frac{1}{2}\Pi_e$.

(iii) 1Q gate G acts on the computational subspace of the erasure qubit, i.e., $G_c \oplus I_e$.

(iv) 2Q gate G acts on the computational subspace of the two erasure qubits and fully depolarizes the other qubit if one qubit is erased, i.e., it applies a quantum channel with Kraus operators $K_{P,Q} = \frac{1}{4} G_{c,c} \oplus P_{c,e} \oplus Q_{e,c} \oplus I_{e,e}$ for all $P, Q \in \{I, X, Y, Z\}$.

(v) 1Q erasure check performs the two-outcome measurement with projectors Π_c and Π_e.

(vi) 1Q reset acts trivially on the computational subspace and reinitializes an erased state as the maximally mixed state in the computational subspace, i.e., it applies a quantum channel with Kraus operators $K_0 = \Pi_c$, $K_1 = \frac{1}{\sqrt{2}}|0\rangle\langle 2|$ and $K_2 = \frac{1}{\sqrt{2}}|1\rangle\langle 2|$.

(vii) 2Q projective measurement measures a Pauli PP operator, but if either qubit is erased, then it gives a random outcome and fully depolarizes the other qubit, i.e., it performs the two-outcome POVM with $\Pi_{PP}^+ + \frac{1}{2}(\Pi_{e,c} + \Pi_{c,e} + \Pi_{e,e})$ and $\Pi_{PP}^- + \frac{1}{2}(\Pi_{e,c} + \Pi_{c,e} + \Pi_{e,e})$ followed by an application of a quantum channel with Kraus operators $K_{P,Q} = \frac{1}{4} I_{c,c} \oplus P_{c,e} \oplus Q_{e,c} \oplus I_{e,e}$ for all $P, Q \in \{I, X, Y, Z\}$.

APPENDIX B: EXAMPLES OF THE EDGE-WEIGHT CALCULATION AND ERASURE RATE ADJUSTMENT

We present an example of how to decode erasures by converting a segment of an erasure circuit into a stabilizer circuit. Consider the segment in Fig. 11(a), where each erasure location has probability e and the erasure check outcome is flipped with probability q. The erasure detection event EC has distribution

$$\Pr(\mathrm{EC} = 1) = [1 - (1 - e)^2](1 - q) + (1 - e)^2 q\,, \tag{B1}$$

$$\Pr(\mathrm{EC} = 0) = 1 - \Pr(\mathrm{EC} = 1)\,. \tag{B2}$$

Conditioned on EC, the probabilities that the qubit was first erased at $\mathcal{E}_1$ or $\mathcal{E}_2$ are, respectively,

$$a_1 = \frac{e(1-q)}{\Pr(\mathrm{EC}=1)}, \quad a_2 = \frac{(1-e)e(1-q)}{\Pr(\mathrm{EC}=1)}\,, \tag{B3}$$

if $D = 1$, and

$$a_1 = \frac{eq}{\Pr(\mathrm{EC}=0)}, \quad a_2 = \frac{(1-e)eq}{\Pr(\mathrm{EC}=0)}\,, \tag{B4}$$

if EC $= 0$. If the qubit was first erased at $\mathcal{E}_1$, it would depolarize the second qubit after the entangling gate. Furthermore, the qubit itself would become maximally mixed after the reset operation. Thus, both qubits become fully depolarized. If the qubit was first erased at $\mathcal{E}_2$, only that qubit would become depolarized from the reset. By the proof of Lemma 1, the segment is equivalent to the stabilizer circuit in Fig. 11(b) with error probabilities

$$b_1' = \frac{15}{16} a_1, \quad b_2' = \frac{3}{4}\frac{a_2}{1-a_1}\,. \tag{B5}$$

To adjust erasure rates at different space-time locations depending on the execution time of quantum circuit operations (and thereby making numerical simulations more realistic) we can use the following simple heuristic. Let T_E be the erasure time (which for the erasure qubit via the dual-rail encoding corresponds to the amplitude damping time T_1). Let $\mathcal{E}$ be an erasure location in-between two consecutive quantum operations A and B with the execution times T_A and T_B, respectively. We can then set the erasure rate associated with $\mathcal{E}$ to be

$$e = (aT_A + bT_B)/T_E\,, \tag{B6}$$

where $a, b \in [0, 1]$ are appropriately chosen. In particular, in the middle of the segment s we may set $a = b = 0.5$; if A or B correspond to one of the end point of s, then we set a or b to be 1. We also remark that adjusting a and b for erasure locations adjacent to erasure checks allows us to effectively adjust the false positive and negative erasure detection rates.

APPENDIX C: PARITY MEASUREMENT OF TWO DUAL-RAIL QUBITS

Here, we outline our scheme for parity measurement of two dual-rail qubits that utilizes a single transmon for measurement. The proposed scheme is based on Fig. 5. The dual-rail qubits are encoded in transmons T1, T2 and T3, T4, respectively, while the interaction is generated by the coupler T5 within the T2, T5, T3 system.

Each dual-rail qubit consists of two tunable transmons, brought to resonance as in Refs. [18,24], while the single tunable transmon T5 realizes the parity measurement. The reason why we can employ such a hybrid construction combining high-coherence dual-rail qubits and a low-coherence transmon is that most of the noise on the ancilla transmon commutes with the interaction, and thereby does not propagate in leading order to the dual-rail qubits as in Ref. [67]. Part of the noise that does propagate is addressed by the dual-rail qubit's built-in decoupling mechanism.

Furthermore, this construction shares similarities with the cavity setup described in Ref. [19]. However, the interaction can be significantly faster than the cavity system since it is not limited by the Purcell effect, which is an important limitation on the rate for high-coherence cavities in a hybrid construction.

The interaction is generated by the second-order ZZ coupling between T5 and T1 and T5 and T3 in the following way. Starting with the Hamiltonian

$$H = \sum_{i=1}^{5} \omega_i a_i^\dagger a_i + \frac{\alpha}{2} a_i^\dagger a_i^\dagger a_i a_i + g_{DR1}(a_1^\dagger a_2 + \text{H.c.}) + g_{DR2}(a_3^\dagger a_4 + \text{H.c.}) + g(a_2^\dagger a_5 + a_5^\dagger a_3 + \text{H.c.}), \tag{C1}$$

where ω_i is the frequency of the transmon Ti, α is the nonlinearity, g_{DRi} is the capacitive coupling between two transmons of the ith dual-rail qubit and g is the capacitive coupling between the ancilla transmon T5 and either T2 or T3.

In the limit of large detunings, $\Delta_1 = \omega_5 - \omega_2$, $\Delta_2 = \omega_5 - \omega_3$, when $\omega_2 = \omega_1$, $\omega_4 = \omega_3$ and $\Delta_i \gg \alpha, g$, the coupling between T5 and the rest of the system reduces to

$$g_{zz}^{(1)} a_5^\dagger a_5 a_2^\dagger a_2 + g_{zz}^{(2)} a_5^\dagger a_5 a_3^\dagger a_3, \tag{C2}$$

when $g_{zz}^i = \frac{g^2}{\Delta_i^2}\alpha$. This Hamiltonian becomes

$$H = \frac{g_{DR1}}{2}\overline{X_1} + \frac{g_{DR2}}{2}\overline{X_2} + a_5^\dagger a_5\left(g_{zz}^{(1)}\overline{Z_1} + g_{zz}^{(2)}\overline{Z_2}\right). \tag{C3}$$

Here, $\overline{Z_i}$ and $\overline{X_i}$ are Pauli operators of the ith dual-rail qubit defined in the standard way for the computational basis states $|0\rangle$ and $|1\rangle$, as defined in Eq. (8). In principle, the interaction terms are off resonance and thus could be neglected unless $g_{zz}^{(i)}$ is modulated at the dual-rail qubit frequency g_{DRi}.

The ZZ coupling term $g_{zz}^{(i)}$ could be modulated by a parametric drive of the detuning resulting in $g_{zz}^i = \frac{g^2}{(\Delta_i + \delta\cos\Omega t)^2}\alpha \approx \frac{g^2}{\Delta_i^2}\alpha - 2\frac{g^2}{\Delta_i^2}\alpha\frac{\delta}{\Delta_i}\cos\Omega t$. Thus, by modulating the coupler frequency, and thus the detuning between the coupler and the dual rails, it is possible to realize an effective Hamiltonian $\frac{g_m}{2}a_5^\dagger a_5\overline{Z_1}$ or $\frac{g_m}{2}a_5^\dagger a_5\overline{Z_2}$. Moreover, by modulating at both frequencies it is possible to realize a Hamiltonian $\frac{g_m}{2}a_5^\dagger a_5(\overline{Z_1} + \overline{Z_2})$. By adding local terms this Hamiltonian could be written as $H_p = \frac{g_m}{2}|f\rangle\langle f|(\overline{Z_1} + \overline{Z_2})$, where $|f\rangle$ denotes the transmon's second excited state. This is exactly what is needed to implement the ZZ gate proposed in Ref. [19]. Here, however, we only aim to use this term to implement a parity measurement, simplifying the scheme and resulting in higher fidelity.

1. Parity measurement scheme

We propose to conduct the parity measurement via the ground state $|g\rangle$ and the second excited state $|f\rangle$ manifold, enabling us to detect amplitude damping of the transmon by measuring the first excited state $|e\rangle$. The protocol starts with the state

$$|g+f\rangle|\alpha\bar{0}\bar{0} + \beta\bar{1}\bar{0} + \gamma\bar{0}\bar{1} + \delta\bar{1}\bar{1}\rangle, \tag{C4}$$

where the basis state of the dual-rail qubit is defined as in Eq. (8). By setting the total time so that $\frac{g}{2}t = \pi$ the unitary $e^{iH_p t}$ propagates the state to

$$|g+f\rangle|\alpha\bar{0}\bar{0} + \delta\bar{1}\bar{1}\rangle + |g-f\rangle|\beta\bar{1}\bar{0} + \gamma\bar{0}\bar{1}\rangle, \tag{C5}$$

which, followed by measuring the operator $|g+f\rangle\langle g+f| - |g-f\rangle\langle g-f|$, realizes the parity measurement. The main advantage of this scheme is that amplitude damping is heralded, and the phase noise of the transmon does not propagate to the dual-rail qubits because the coupling term $a_5^\dagger a_5$ commutes with the noise term. Thus, the transmon's phase noise only affects the measurement error, benefiting from a large threshold, as discussed in Ref. [67]. This property of the measurement scheme allows for the utilization of a low-coherence single transmon and does not necessitate the use of a dual-rail qubit as an ancilla or a coupler, which would have slowed down the protocol considerably.

The parity measurement itself is slower by a factor of 2 than the regular ZZ term between two transmons and the gate should be realized twice, once for each dual rail. The gate itself could be achieved at around 80 ns as shown in Fig. 13. The dephasing due to the dual-rail qubit would be of the order of $\sim 2 \times \frac{80\,\text{ns}}{2.5\,\text{ms}} \sim 3 \times 10^{-5}$ for each parity measurement, for the Markovian case and down to the 10^{-9} level for the non Markovian one, where the estimation of the 2.5 ms coherence time is based on results in Ref. [24]. Thus, the main source of dephasing would be the erasure measurements. The erasure measurement takes a similar amount of time as a regular measurement, which could be performed in less than 100 ns [68] or even below 50 ns [69], which is comparable to the gate time. Thus, we anticipate that the measurement-induced dephasing will be the main source of noise in this scheme and should be of the order of 10^{-4} [24]. Since the erasure measurement could, in principle, be realized in parallel with the gate implementation, the erasure measurement may not incur an additional cost in terms of fidelity. Therefore, the blue solid line should coincide with the blue dashed line in Fig. 6(e).

The low transmon's coherence will only limit the measurement fidelity to the level of $\sim\frac{160\,\text{ns}}{T_2} \sim 0.5\%$, where 160 ns is the parity measurement time, which is not a real limitation as measurement fidelities are already limited to that level due measurement errors.

The gate speed will be limited by the off-resonant error terms which will cause leakage at the end of the gate. These transitions are shown in Fig. 12. As these transitions are detuned by $\frac{\omega_T - g_{DR}}{2}$, where ω_T is the transmon frequency and g_{DR} is the dual-rail gap, the error terms are approximately $\frac{8}{((\omega_T - g_{DR})T_g)^4}$ [70]. Assuming we target a fidelity of around 10^{-4} the gate time should be of the order of 40 ns.

We numerically validate the analytical estimate of the parity-check fidelity, as shown in Fig. 13. We employed a one-parameter pulse shape for the detuning modulation envelope, given by $\cos(t\omega)(1 - [1 - \sin(\frac{\pi t}{\text{Tt}})]^m)^m$, where T is an optimization parameter and we set $m = 6$. Using this configuration, a fidelity of 10^{-3} was achieved. By increasing the

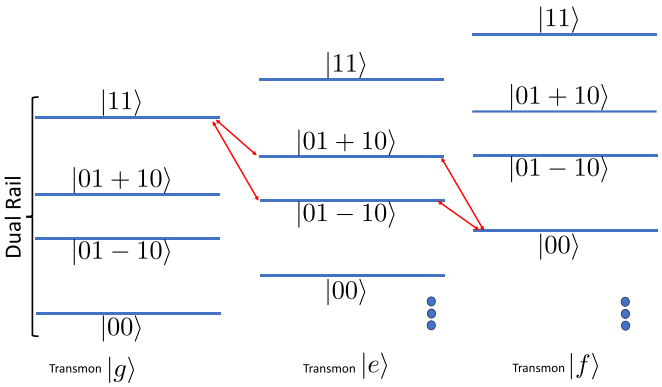


FIG. 12. Error terms that restrict the accuracy of the parity measurements are illustrated. The level structure of the dual-rail qubit is depicted in each column based on the ancilla transmon state, which can be either $|g\rangle$, $|e\rangle$, or $|f\rangle$. When inducing a transition between the states $|01+10\rangle$ and $|01-10\rangle$ by modulating the detuning, unwanted couplings, highlighted in red, will cause leakage and constrain the gate fidelity.

number of optimization parameters, both the fidelity and the pulse time are expected to improve considerably.

APPENDIX D: ERASURE PROPAGATION

Now, we discuss the justification for the different error spread models for dual-rail qubits. We start with the typical ancilla-based code operations. Here, both the qubits and the ancillas are implemented using a dual-rail system, and the gate connecting them follows the method proposed in Ref. [18]. This gate exploits a flip-flop interaction between the dual-rail qubits, which is randomly halted when one of them is erased. Since the erasure check does not provide the exact time of the decay, the flip-flop interaction creates a mixture of the original state and the dephased state on the unerased qubit, which we assume to be random. Tracing out the erased qubit, this realizes the channel $\rho \mapsto \frac{1}{2}\rho + \frac{1}{4}I$. We use the fully depolarizing channel to give an upper bound on its performance.

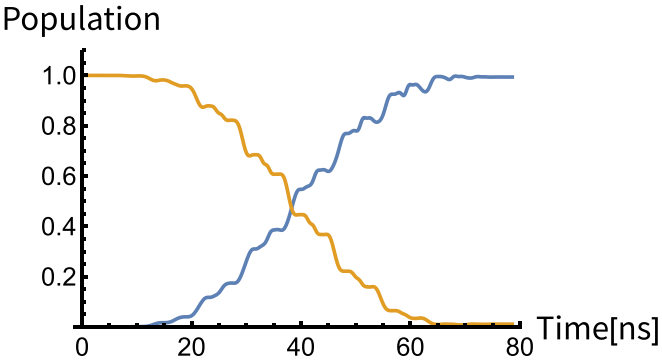


FIG. 13. Simulation of one-half of a parity check, i.e., a state-dependent 2π rotation of the dual-rail qubit conditioned on the state of the coupler. The simulation is done for a GHz detuning between the dual-rail qubit and the ancilla, coupling of 270 MHz and the dual-rail coupling of 145 MHz. The figure shows oscillations between $|f\rangle|\bar{0}+\bar{1}\rangle$ (yellow) to $|f\rangle|\bar{0}-\bar{1}\rangle$ (blue) and back, the final state acquires a π phase with respect to the initial state.

A more rigorous derivation is the following. The erasure process is an exponential process with parameter T_1. As the gate time is much shorter than T_1, we can approximate it by a homogeneous distribution, giving the channel

$$\mathrm{Tr}_1\left[\frac{1}{\pi}\int_0^{\pi} e^{-i\theta(\sigma_+^1\sigma_-^2+\mathrm{H.c.})}\rho e^{+i\theta(\sigma_+^1\sigma_-^2+\mathrm{H.c.})}d\theta\right], \tag{D1}$$

where $\sigma_\pm^i$ are the raising and lowering operators within the dual-rail basis of the ith qubit and the trace operation is over the erased qubit, which we assume to be the first qubit. This expression evaluates to $\rho_{00,11} + \frac{1}{2}[\rho - (\sigma_+^1\sigma_-^2 + \mathrm{H.c.})\rho(\sigma_+^1\sigma_-^2 + \mathrm{H.c.})]_{01,10}$, where the first part is the density matrix of the 00, 11 subspace and the second part, the 01, 10 subspace. Assuming that we do not have information on the erased state, this gives the channel $\frac{1}{2}\rho + \frac{1}{4}I$.

Note that the argument above clarifies why an erasure happening during a two-qubit gate propagates as depolarization. An erasure that takes place before the two-qubit gate could propagate either as a depolarizing error or as a distinct Z or X error, depending on the gate. In this context, we still assume it spreads as a depolarizing error, which is the worst-case scenario. In the case of a direct ZZ interaction between the dual-rail bases, the channel was calculated in Ref. [40].

Next, we discuss EM scheme as depicted in Fig. 5. This scheme involves coupling the ancilla to the dual-rail qubits through a Z-type interaction. Consequently, only phase noise resulting from erasure in one of the dual-rail qubits will be inflicted on the ancilla. This phase noise does not propagate to the other dual-rail qubit and results solely in a measurement error. In second order, the ancilla can be adiabatically eliminated, leaving the two dual-rail qubits with a flip-flop interaction. This interaction may lead to the propagation of both erasure-erasure and erasure-Pauli errors.

In the case that the transmons of both dual-rail qubits are off resonant, a ZZ interaction between the transmons triggers a Pauli spread mechanism. Using the notation from Fig. 5 and Appendix C, a ZZ interaction occurs between transmons T2 and T3, manifesting as a flip-flop interaction in the dual-rail basis. An erasure during the gate will halt this interaction, effectively introducing a noise mechanism. As in the ancilla-based code this realizes the channel $\frac{1}{2}\rho + \frac{1}{4}I$.

In various scenarios when trying to increase the interaction between the two dual-rail qubits, it could be advantageous to bring them closer to resonance. In such a scenario, erasure transfers between the dual-rail qubits, i.e., swapping the excitation in one dual-rail qubit to the erased qubit, would be a significant error propagation mechanism. Ideally, this would result in a total exchange between the qubits, with the other qubit trading its state with the erased one. However, this only occurs when all dual-rail qubit parameters are precisely matched, a regime which is not interesting for realizing fast gates. Thus, the channel that propagates erasure and depolarizes the other dual-rail qubit is a reasonable choice capturing the detrimental effects of the real channel.

APPENDIX E: DETAILS OF NUMERICAL SIMULATIONS

We present more details on how the simulations were performed. For a given circuit, the state is initialized as the eigenstate of a chosen logical operator, and an error is reported

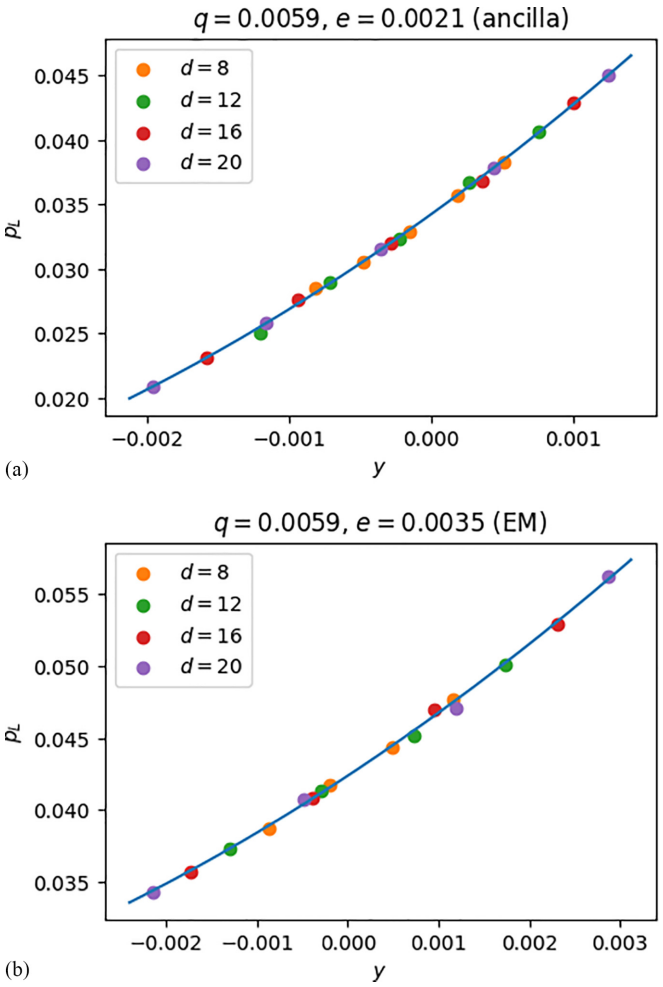


FIG. 14. Rescaled data for the sample threshold calculations in Fig. 6 based on Eqs. (E1) and (E2), where $y = p$ is the swept variable. (a) Sample calculation for the ancilla scheme threshold, giving $y^* = 9.1 \times 10^{-4}$, $\alpha = 0.97$, and the quadratic $p_L = 570y^2 + 7.9y + 0.034$. (b) Sample calculation for the EM scheme threshold, giving $y^* = 1.8 \times 10^{-3}$, $\alpha = 0.99$, and the quadratic $p_L = 210y^2 + 4.2y + 0.042$.

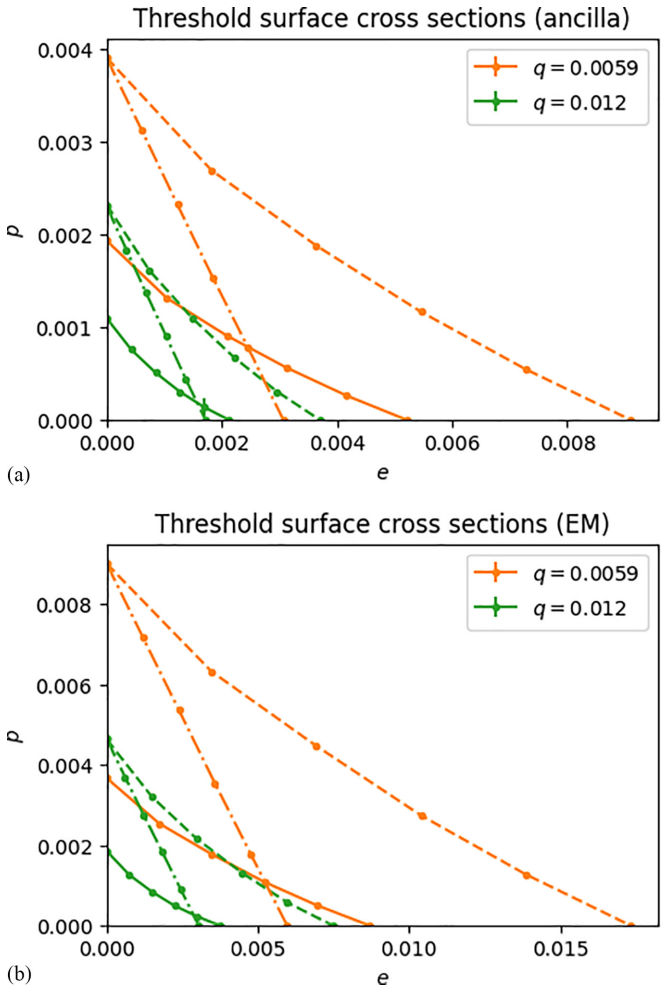


FIG. 15. Cross sections of the threshold surfaces from Fig. 6 for different values of q (solid lines) for the (a) ancilla and (b) EM schemes. The dashed lines correspond to the scheme with erasure checks and reset that do not introduce additional errors, bounding the performance of any erasure scheme. The dashed-dotted lines correspond to the standard scheme with no erasure checks and ideal reset (which can also be interpreted as the code's performance under leakage).

if the logical operator is decoded to the wrong value at the end of the simulation.[4] Because we are interested in threshold values, we assume perfect initialization and a noiseless final measurement. We run the simulation for $9d$ noisy measurement rounds for $d = 4, 8, 12, 16, 20$ to obtain p'_L, and then report the normalized error rate per $3d$ rounds calculated via $p_L = \frac{1}{2}[1 - (1 - 2p'_L)^{1/3}] \approx p'_L/3$. The logical error rate p_L is calculated as the average over at least 1000 circuit realizations (from a given pattern of erasure check detection events), where each circuit realization is sampled 200 times. Examples of different circuit realizations, as well as an interactive circuit diagram, can be found in [71].

The threshold surfaces in Fig. 6 are obtained by sweeping an error parameter (usually p, but sometimes q or e for points where $p = 0$) in the neighborhood of a suspected threshold point in the (e, p, q) phase space. The threshold value is estimated by fitting the universal scaling ansatz for critical points of phase transitions [72,73]. That is, around the threshold, we assume the form

$$p_L = ax^2 + bx + c \tag{E1}$$

for the scaled variable

$$x = (y - y^*)d^\alpha\,, \tag{E2}$$

where p_L is the logical error rate, $y \in \{e, p, q\}$ is the swept error variable, and a, b, c, y^*, α are fitting parameters; see Fig. 14 for example calculations. In Fig. 15, we present additional cross sections of the threshold surfaces from Fig. 6.

[4]Because Floquet codes encode two logical qubits, the word error rate is four times the values presented if we assume independent X and Z failure probabilities. The thresholds will remain the same.

[1] P. W. Shor, Scheme for reducing decoherence in quantum computer memory, Phys. Rev. A **52**, R2493 (1995).

[2] A. M. Steane, Error correcting codes in quantum theory, Phys. Rev. Lett. **77**, 793 (1996).

[3] P. Shor, Fault-tolerant quantum computation, in *Proceedings of 37th Conference on Foundations of Computer Science* (IEEE Computer Society Press, Washington, DC, 1996), pp. 56–65.

[4] P. T. Cochrane, G. J. Milburn, and W. J. Munro, Macroscopically distinct quantum-superposition states as a bosonic code for amplitude damping, Phys. Rev. A **59**, 2631 (1999).

[5] M. Mirrahimi, Z. Leghtas, V. V. Albert, S. Touzard, R. J. Schoelkopf, L. Jiang, and M. H. Devoret, Dynamically protected cat-qubits: A new paradigm for universal quantum computation, New J. Phys. **16**, 045014 (2014).

[6] N. Ofek, A. Petrenko, R. Heeres, P. Reinhold, Z. Leghtas, B. Vlastakis, Y. Liu, L. Frunzio, S. Girvin, L. Jiang *et al.*, Extending the lifetime of a quantum bit with error correction in superconducting circuits, Nature (London) **536**, 441 (2016).

[7] S. Puri, A. Grimm, P. Campagne-Ibarcq, A. Eickbusch, K. Noh, G. Roberts, L. Jiang, M. Mirrahimi, M. H. Devoret, and S. M. Girvin, Stabilized cat in a driven nonlinear cavity: A fault-tolerant error syndrome detector, Phys. Rev. X **9**, 041009 (2019).

[8] J. Guillaud and M. Mirrahimi, Repetition cat qubits for fault-tolerant quantum computation, Phys. Rev. X **9**, 041053 (2019).

[9] D. K. Tuckett, S. D. Bartlett, and S. T. Flammia, Ultrahigh error threshold for surface codes with biased noise, Phys. Rev. Lett. **120**, 050505 (2018).

[10] D. K. Tuckett, A. S. Darmawan, C. T. Chubb, S. Bravyi, S. D. Bartlett, and S. T. Flammia, Tailoring surface codes for highly biased noise, Phys. Rev. X **9**, 041031 (2019).

[11] D. K. Tuckett, S. D. Bartlett, S. T. Flammia, and B. J. Brown, Fault-tolerant thresholds for the surface code in excess of 5% under biased noise, Phys. Rev. Lett. **124**, 130501 (2020).

[12] J. P. Bonilla Ataides, D. K. Tuckett, S. D. Bartlett, S. T. Flammia, and B. J. Brown, The XZZX surface code, Nat. Commun. **12**, 2172 (2021).

[13] A. Dua, A. Kubica, L. Jiang, S. T. Flammia, and M. J. Gullans, Clifford-deformed surface codes, PRX Quantum **5**, 010347 (2024).

[14] Q. Xu, N. Mannucci, A. Seif, A. Kubica, S. T. Flammia, and L. Jiang, Tailored XZZX codes for biased noise, Phys. Rev. Res. **5**, 013035 (2023).

[15] O. Higgott, T. C. Bohdanowicz, A. Kubica, S. T. Flammia, and E. T. Campbell, Improved decoding of circuit noise and fragile boundaries of tailored surface codes, Phys. Rev. X **13**, 031007 (2023).

[16] Y. Wu, S. Kolkowitz, S. Puri, and J. D. Thompson, Erasure conversion for fault-tolerant quantum computing in alkaline earth Rydberg atom arrays, Nat. Commun. **13**, 4657 (2022).

[17] M. Kang, W. C. Campbell, and K. R. Brown, Quantum error correction with metastable states of trapped ions using erasure conversion, PRX Quantum **4**, 020358 (2023).

[18] A. Kubica, A. Haim, Y. Vaknin, H. Levine, F. Brandão, and A. Retzker, Erasure qubits: Overcoming the T_1 limit in superconducting circuits, Phys. Rev. X **13**, 041022 (2023).

[19] J. D. Teoh, P. Winkel, H. K. Babla, B. J. Chapman, J. Claes, S. J. de Graaf, J. W. O. Garmon, W. D. Kalfus, Y. Lu, A. Maiti, K. Sahay, N. Thakur, T. Tsunoda, S. H. Xue, L. Frunzio, S. M. Girvin, S. Puri, and R. J. Schoelkopf, Dual-rail encoding with superconducting cavities, Proc. Natl. Acad. Sci. USA **120**, e2221736120 (2023).

[20] A. M. Kubica and A. Retzker, Heralding of amplitude damping decay noise for quantum error correction, 2023, US Patent No. 11,748,652.

[21] S. Ma, G. Liu, P. Peng, B. Zhang, S. Jandura, J. Claes, A. P. Burgers, G. Pupillo, S. Puri, and J. D. Thompson, High-fidelity gates and mid-circuit erasure conversion in an atomic qubit, Nature (London) **622**, 279 (2023).

[22] P. Scholl, A. L. Shaw, R. B.-S. Tsai, R. Finkelstein, J. Choi, and M. Endres, Erasure conversion in a high-fidelity Rydberg quantum simulator, Nature (London) **622**, 273 (2023).

[23] K. S. Chou, T. Shemma, H. McCarrick, T.-C. Chien, J. D. Teoh, P. Winkel, A. Anderson, J. Chen, J. Curtis, S. J. de Graaf *et al.*, A superconducting dual-rail cavity qubit with erasure-detected logical measurements, Nat. Phys. **20**, 1454 (2024).

[24] H. Levine, A. Haim, J. S. C. Hung, N. Alidoust, M. Kalaee, L. DeLorenzo, E. A. Wollack, P. Arrangoiz-Arriola, A. Khalajhedayati, R. Sanil, H. Moradinejad, Y. Vaknin, A. Kubica, D. Hover, S. Aghaeimeibodi, J. A. Alcid, C. Baek, J. Barnett, K. Bawdekar, P. Bienias *et al.*, Demonstrating a long-coherence dual-rail erasure qubit using tunable transmons, Phys. Rev. X **14**, 011051 (2024).

[25] A. Koottandavida, I. Tsioutsios, A. Kargioti, C. R. Smith, V. R. Joshi, W. Dai, J. D. Teoh, J. C. Curtis, L. Frunzio, R. J. Schoelkopf, and M. H. Devoret, Erasure detection of a dual-rail qubit encoded in a double-post superconducting cavity, arXiv:2311.04423.

[26] M. Grassl, T. Beth, and T. Pellizzari, Codes for the quantum erasure channel, Phys. Rev. A **56**, 33 (1997).

[27] T. M. Stace, S. D. Barrett, and A. C. Doherty, Thresholds for topological codes in the presence of loss, Phys. Rev. Lett. **102**, 200501 (2009).

[28] N. Delfosse and N. H. Nickerson, Almost-linear time decoding algorithm for topological codes, Quantum **5**, 595 (2021).

[29] K. Sahay, J. Jin, J. Claes, J. D. Thompson, and S. Puri, High-threshold codes for neutral-atom qubits with biased erasure errors, Phys. Rev. X **13**, 041013 (2023).

[30] E. Dennis, A. Kitaev, A. Landahl, and J. Preskill, Topological quantum memory, J. Math. Phys. **43**, 4452 (2002).

[31] M. B. Hastings and J. Haah, Dynamically generated logical qubits, Quantum **5**, 564 (2021).

[32] J. Haah and M. B. Hastings, Boundaries for the honeycomb code, Quantum **6**, 693 (2022).

[33] I. L. Chuang and Y. Yamamoto, Simple quantum computer, Phys. Rev. A **52**, 3489 (1995).

[34] R. Duan, M. Grassl, Z. Ji, and B. Zeng, Multi-error-correcting amplitude damping codes, in *Proceedings of the 2010 IEEE International Symposium on Information Theory* (IEEE, Piscataway, NJ, 2010), pp. 2672–2676.

[35] D. Gottesman, The Heisenberg representation of quantum computers, in *Proceedings of the XXII International Colloquium on Group Theoretical Methods in Physics, 1998* (International Press, Boston, 1998), pp. 32–43.

[36] S. Aaronson and D. Gottesman, Improved simulation of stabilizer circuits, Phys. Rev. A **70**, 052328 (2004).

[37] P. Aliferis and B. M. Terhal, Fault-tolerant quantum computation for local leakage faults, Quantum Inf. Comput. **7**, 139 (2007).

[38] B. M. Varbanov, F. Battistel, B. M. Tarasinski, V. P. Ostroukh, T. E. O'Brien, L. DiCarlo, and B. M. Terhal, Leakage detection for a transmon-based surface code, npj Quantum Inf. **6**, 102 (2020).

[39] K. C. Miao, M. McEwen, J. Atalaya, D. Kafri, L. P. Pryadko, A. Bengtsson, A. Opremcak, K. J. Satzinger, Z. Chen, P. V. Klimov, C. Quintana, R. Acharya, K. Anderson, M. Ansmann, F. Arute, K. Arya, A. Asfaw, J. C. Bardin, A. Bourassa, J. Bovaird *et al.*, Overcoming leakage in quantum error correction, Nat. Phys. **19**, 1780 (2023).

[40] S. Gu, Y. Vaknin, A. Retzker, and A. Kubica, Optimizing quantum error correction protocols with erasure qubits, arXiv:2408.00829.

[41] C. Gidney, Stim: A fast stabilizer circuit simulator, Quantum **5**, 497 (2021).

[42] E. Berlekamp, R. McEliece, and H. van Tilborg, On the inherent intractability of certain coding problems (corresp.), IEEE Trans. Inf. Theory **24**, 384 (1978).

[43] D. S. Wang, A. G. Fowler, C. D. Hill, and L. C. L. Hollenberg, Graphical algorithms and threshold error rates for the 2d color code, Quantum Inf. Comput. **10**, 780 (2010).

[44] N. Delfosse, A. Paetznick, J. Haah, and M. B. Hastings, Splitting decoders for correcting hypergraph faults, arXiv:2309.15354.

[45] R. Chao, M. E. Beverland, N. Delfosse, and J. Haah, Optimization of the surface code design for Majorana-based qubits, Quantum **4**, 352 (2020).

[46] J. Edmonds, Paths, trees, and flowers, Can. J. Math. **17**, 449 (1965).

[47] F. Yan, D. Campbell, P. Krantz, M. Kjaergaard, D. Kim, J. L. Yoder, D. Hover, A. Sears, A. J. Kerman, T. P. Orlando, S. Gustavsson, and W. D. Oliver, Distinguishing coherent and thermal photon noise in a circuit quantum electrodynamical system, Phys. Rev. Lett. **120**, 260504 (2018).

[48] J. J. Burnett, A. Bengtsson, M. Scigliuzzo, D. Niepce, M. Kudra, P. Delsing, and J. Bylander, Decoherence benchmarking of superconducting qubits, npj Quantum Inf. **5**, 54 (2019).

[49] C. Gidney, M. Newman, and M. McEwen, Benchmarking the planar honeycomb code, Quantum **6**, 813 (2022).

[50] M. Davydova, N. Tantivasadakarn, and S. Balasubramanian, Floquet codes without parent subsystem codes, PRX Quantum **4**, 020341 (2023).

[51] Z. Zhang, D. Aasen, and S. Vijay, The x-cube floquet code, arXiv:2211.05784.

[52] M. S. Kesselring, J. C. Magdalena de la Fuente, F. Thomsen, J. Eisert, S. D. Bartlett, and B. J. Brown, Anyon condensation and the color code, PRX Quantum **5**, 010342 (2024).

[53] M. Davydova, N. Tantivasadakarn, S. Balasubramanian, and D. Aasen, Quantum computation from dynamic automorphism codes, Quantum **8**, 1448 (2024).

[54] A. Dua, N. Tantivasadakarn, J. Sullivan, and T. D. Ellison, Engineering 3d floquet codes by rewinding, PRX Quantum **5**, 020305 (2024).

[55] O. Higgott and N. P. Breuckmann, Constructions and performance of hyperbolic and semi-hyperbolic Floquet codes, PRX Quantum **5**, 040327 (2024).

[56] A. Fahimniya, H. Dehghani, K. Bharti, S. Mathew, A. J. Kollár, A. V. Gorshkov, and M. J. Gullans, Fault-tolerant hyperbolic floquet quantum error correcting codes, arXiv:2309.10033.

[57] J. C. M. de la Fuente, J. Old, A. Townsend-Teague, M. Rispler, J. Eisert, and M. Müller, The XYZ ruby code: Making a case for a three-colored graphical calculus for quantum error correction in spacetime, arXiv:2407.08566.

[58] O. Higgott and C. Gidney, Sparse blossom: Correcting a million errors per core second with minimum-weight matching, arXiv:2303.15933.

[59] C. Gidney, M. Newman, A. Fowler, and M. Broughton, A fault-tolerant honeycomb memory, Quantum **5**, 605 (2021).

[60] H. Bombin and M. A. Martin-Delgado, Optimal resources for topological two-dimensional stabilizer codes: Comparative study, Phys. Rev. A **76**, 012305 (2007).

[61] H. Bombin and M. A. Martin-Delgado, Topological quantum distillation, Phys. Rev. Lett. **97**, 180501 (2006).

[62] A. M. Kubica, The ABCs of the Color Code: A study of topological quantum codes as toy models for Fault-Tolerant quantum computation and quantum phases of matter, Ph.D. thesis, California Institute of Technology, 2018.

[63] N. P. Breuckmann and J. N. Eberhardt, Quantum low-density parity-check codes, PRX Quantum **2**, 040101 (2021).

[64] C. Gidney, A pair measurement surface code on pentagons, Quantum **7**, 1156 (2023).

[65] S. Bravyi, A. W. Cross, J. M. Gambetta, D. Maslov, P. Rall, and T. J. Yoder, High-threshold and low-overhead fault-tolerant quantum memory, arXiv:2308.07915.

[66] Q. Xu, J. P. B. Ataides, C. A. Pattison, N. Raveendran, D. Bluvstein, J. Wurtz, B. Vasic, M. D. Lukin, L. Jiang, and H. Zhou, Constant-overhead fault-tolerant quantum computation with reconfigurable atom arrays, arXiv:2308.08648.

[67] I. Zuk, D. Cohen, A. V. Gorshkov, and A. Retzker, Robust gates with spin-locked superconducting qubits, Phys. Rev. Res. **6**, 013217 (2024).

[68] J. Heinsoo, C. K. Andersen, A. Remm, S. Krinner, T. Walter, Y. Salathé, S. Gasparinetti, J.-C. Besse, A. Potočnik, A. Wallraff *et al.*, Rapid high-fidelity multiplexed readout of superconducting qubits, Phys. Rev. Appl. **10**, 034040 (2018).

[69] Y. Sunada, K. Yuki, Z. Wang, T. Miyamura, J. Ilves, K. Matsuura, P. A. Spring, S. Tamate, S. Kono, and Y. Nakamura, Photon-noise-tolerant dispersive readout of a superconducting qubit using a nonlinear purcell filter, PRX Quantum **5**, 010307 (2024).

[70] I. I. Boradjiev and N. V. Vitanov, Control of qubits by shaped pulses of finite duration, Phys. Rev. A **88**, 013402 (2013).

[71] S. Gu, Data for "Fault-tolerant quantum architectures based on erasure qubits", [Data set] Zenodo (2024), doi:10.5281/zenodo.13730128.

[72] C. Wang, J. Harrington, and J. Preskill, Confinement-higgs transition in a disordered gauge theory and the accuracy threshold for quantum memory, Ann. Phys. **303**, 31 (2003).

[73] J. W. Harrington, Analysis of quantum error-correcting codes: Symplectic lattice codes and toric codes, Ph.D. thesis, California Institute of Technology, 2004.